

# Reconstructing the cosmic density field with the distribution of dark matter halos

Huiyuan Wang<sup>1,2,4\*</sup>, H.J. Mo<sup>1</sup>, Y.P. Jing<sup>3,4</sup>, Yicheng Guo<sup>1</sup>, Frank C. van den Bosch<sup>5</sup> and Xiaohu Yang<sup>3,4</sup>

<sup>1</sup>*Department of Astronomy, University of Massachusetts, Amherst MA 01003-9305, USA*

<sup>2</sup>*Center for Astrophysics, University of Science and Technology of China, Hefei, Anhui, China*

<sup>3</sup>*Shanghai Astronomical Observatory; the Partner Group of MPA, Nandan Road 80, Shanghai 200030, China*

<sup>4</sup>*Joint Institute for Galaxy and Cosmology (JOINGC) of SHAO and USTC*

<sup>5</sup>*Max-Planck-Institute for Astronomy, Königstuhl 17, D-69117 Heidelberg, Germany*

Accepted ..... Received .....; in original form .....

## ABSTRACT

We develop a new method to reconstruct the cosmic density field from the distribution of dark matter haloes above a certain mass threshold. Our motivation is that well-defined samples of galaxy groups/clusters, which can be used to represent the dark halo population, can now be selected from large redshift surveys of galaxies, and our ultimate goal is to use such data to reconstruct the cosmic density field in the local universe. Our reconstruction method starts with a sample of dark matter haloes above a given mass threshold. Each volume element in space is assigned to the domain of the nearest halo according to a distance measure that is scaled by the virial radius of the halo. The distribution of the mass in and around dark matter haloes of a given mass is modelled using the cross-correlation function between dark matter haloes and the mass distribution within their domains. We use N-body cosmological simulations to show that the density profiles required in our reconstruction scheme can be determined reliably from large cosmological simulations, and that our method can reconstruct the density field accurately using haloes with masses down to  $\sim 10^{12} h^{-1} M_{\odot}$  (above which samples of galaxy groups can be constructed from current large redshift surveys of galaxies). Working in redshift space, we demonstrate that the redshift distortions due to the peculiar velocities of haloes can be corrected in an iterative way. We also describe some applications of our method.

**Key words:** dark matter - large-scale structure of the universe - galaxies:  
haloes - methods: statistical

## 1 INTRODUCTION

There is now much evidence that we live in a flat universe dominated by cold dark matter (CDM,  $\sim 30\%$ ) and dark energy ( $\sim 70\%$ ). In addition, perturbations in the density field are characterized by an initial power spectrum with a spectral index  $n \sim 1$ , and a normalization  $\sigma_8 \sim 0.8$ . Here  $\sigma_8$  is the *RMS* of the linear perturbation field at the present, in spheres of  $8 h^{-1}\text{Mpc}$  radius. This ‘standard’  $\Lambda\text{CDM}$  model has been very successful in explaining a variety of observations, such as temperature fluctuations in the cosmic microwave background, the clustering of galaxies on large scales, and the clustering of the Lyman- $\alpha$  forest at high redshift (e.g. Spergel et al, 2007 and references therein). In the CDM cosmogony, a key concept in the build-up of structure is the formation of dark matter haloes, formed through non-linear gravitational collapse. In a hierarchical scenario like CDM, most of the mass at any given time is bound within dark haloes of various masses; galaxies and other luminous objects are assumed to form by cooling and condensation of baryonic gas within these haloes (e.g. White & Rees 1978). With current N-body simulations and analytic models, the properties of the CDM halo population, such as the mass function, the spatial clustering, the formation history and the internal structure are well understood. However, the details of how galaxies form in the cosmic density field are still poorly understood.

A key step in understanding galaxy formation in the cosmic density field is to understand the relationships between galaxies, dark matter haloes and the large scale structure. The study of the large-scale structure in the universe typically relies on large redshift surveys of galaxies, such as the Sloan Digital Sky Survey (hereafter SDSS, e.g. York et al. 2000) and the 2-degree Galaxy Redshift Survey (2dFGRS, e.g. Colless et al. 2001). However galaxies are known to be biased tracers of the large scale mass distribution. Unfortunately, the exact form of this bias is complicated, as it depends on various properties of the galaxies, such as luminosity and color. Gravitational lensing and X-ray observations may be used to probe the mass distribution in individual massive systems (see the review of Bartelmann & Schneider 2001; Evrard, Metzler, Navarro 1996; Gastaldello et al. 2007), such as clusters, but the majority of the mass, which is contained in systems of lower masses, cannot be probed

\* E-mail: whywang@mail.ustc.edu.cn

in this way. On super-cluster scales, gravitational weak lensing can be used to study the properties of the mass distribution in a statistical way, but it is still difficult to use this method to directly identify the large-scale structure in detail.

One important development in recent years is that tremendous amounts of effort have been put into the establishment of the relationship between galaxies and dark matter haloes, using numerical simulations (e.g., Katz, Weinberg & Hernquist 1996; Pearce et al. 2000; Springel 2005; Springel et al. 2005) or semi-analytical models (e.g. White & Frenk 1991; Kauffmann et al. 1993, 2004; Somerville & Primack 1999; Cole et al. 2000; van den Bosch 2002; Kang et al. 2005; Croton et al. 2006). Both of these techniques try to model the process of galaxy formation *ab initio*. However, since our understanding of the various physical processes involved is still relatively poor, the relations between the properties of galaxies and their dark matter haloes predicted by these simulations and semi-analytical models still need to be tested against observations. More recently, the halo occupation model has opened another avenue to probe the galaxy-dark matter halo connection (e.g. Jing, Mo & Börner 1998; Peacock & Smith 2000; Berlind & Weinberg 2002; Cooray & Sheth 2002; Scranton 2003; Yang, Mo & van den Bosch 2003; van den Bosch, Yang & Mo 2003; Yan, Madgwick & White 2003; Tinker et al. 2005; Zheng et al. 2005; Cooray 2006; Vale & Ostriker 2006; van den Bosch et al. 2007). This technique uses the observed galaxy luminosity function and two-point correlation functions to constrain the average number of galaxies of given properties that occupy a dark matter halo of given mass. Although this method has the advantage that it can yield much better fits to the data than the semi-analytical models or numerical simulations, one typically needs to assume a somewhat ad-hoc functional form to describe the halo occupation model. A more direct way of studying the galaxy-halo connection is by using galaxy groups, provided that these are defined as sets of galaxies that reside in the same dark matter halo. Recently, Yang et al. (2005; 2007) have developed a halo-based group finder that is optimized for grouping galaxies that reside in the same dark matter halo. Using mock galaxy redshift surveys constructed from the conditional luminosity function model (e.g. Yang, Mo & van den Bosch 2003) and a semi-analytical model (Kang et al, 2005), it is found that this group finder is very successful in associating galaxies with their common dark matter haloes (see Yang et al. 2007). The group finder also performs reliably for poor systems, including isolated galaxies in small mass haloes, making it ideally suited for the study of the relation between galaxies and dark matter haloes over a wide range of halo

masses. Thus far, this halo-based group finder has been applied to 2dFGRS (Yang et al. 2005), SDSS DR2 (Weinmann et al. 2006) and SDSS DR4 (Yang et al. 2007).

In the current CDM model, the relationship between dark haloes and the mass density field can be understood using  $N$ -body simulations and/or analytical models. This relationship, together with the galaxy groups that represent dark haloes, offers the possibility to reconstruct the underlying cosmic density field with the use of the dark haloes represented by galaxy systems. If this approach proves successful, its applications to real observations will enable us to map the density field in the local universe, allowing us to study in detail the relationships between galaxies, dark haloes and large-scale structure. In this paper we develop a method to reconstruct the cosmic density field from the distribution of dark matter haloes. Our method uses the fact that the statistical properties of the large-scale structure are well represented by the current  $\Lambda$ CDM model and that dark haloes can be selected reliably from large redshift surveys of galaxies, as mentioned above.

The reconstruction of the cosmic density field from galaxy distribution has been carried out earlier based on various redshift surveys (e.g. Fisher et al. 1995; Zaroubi et al. 1995; Schmoldt et al. 1999; Mathis et al. 2002; Erdoğan et al. 2004). In these investigations, the distribution of galaxies is usually smoothed heavily and normalized to represent the cosmic density field on large scales. In the Wiener reconstruction method adopted in many of the earlier investigations, the mass density at a given point is assumed to be a linear combination of the observed galaxy density field values at different points so that the reconstructed field has the minimum mean square error. Our method is different from these methods in that it is based on dark matter haloes so that the reconstruction is more accurate on small scales. Furthermore, since our method is based on dark matter haloes represented by galaxy systems, the bias of the distributions of different galaxies relative to the underlying density field is automatically taken into account by their connections to dark matter haloes.

This paper is arranged as follows. We describe briefly the simulations to be used and how dark haloes are identified in Section 2. In Section 3 we present our reconstruction method and calculate the density profiles within and around haloes of different masses. In Section 4 we compare our density field reconstructed from the halo catalogue selected from the simulations with the original density field. In Section 5 we examine how our reconstruction scheme works in redshift space. In Section 6 we outline some potential applications of our method, and we summarize our results in Section 7.

## 2 SIMULATIONS

In this paper, we use two sets of  $N$ -body simulations and dark matter haloes selected from them to test the reconstruction method we propose. Here we give a brief description of these two simulations. These simulations are obtained using the P<sup>3</sup>M code described in Jing & Suto (2002). The main simulation, which will be referred to as L300, assumes a spatially-flat  $\Lambda$ CDM model, with density parameters  $\Omega_m = 0.3$  and  $\Omega_\Lambda = 0.7$ , and with the CDM power spectrum given by Bardeen et al (1986), with a shape parameter  $\Gamma = \Omega_m h = 0.2$  and an amplitude specified by  $\sigma_8 = 0.9$ . The CDM density field was traced with  $512^3$  particles, each having a mass of  $M_p \sim 1.68 \times 10^{10} h^{-1} M_\odot$ , in a cubic box of  $300 h^{-1} \text{Mpc}$ . The softening length is  $\sim 30 h^{-1} \text{kpc}$ . The other simulation, referred to as L100 in the following, assumes the same cosmological model as L300, and uses the same number of particles, but the simulation box is smaller,  $100 h^{-1} \text{Mpc}$ , and the mass resolution is higher,  $M_p \sim 6.2 \times 10^8 h^{-1} M_\odot$ .

Dark matter haloes were identified with a friends-of-friends algorithm with a link length that is 0.2 times the mean particles separation. The mass of a halo,  $M_h$ , is the sum of the mass of all the particles in the halo. The virial radius  $R_h$  of a halo is defined as:

$$R_h = \left( \frac{3M_h}{4\pi\Delta_h\rho_m} \right)^{1/3}, \quad (1)$$

where  $\rho_m$  is the mean mass density of the universe, and  $\Delta_h$  is the mean density contrast of a virialized halo. We choose  $\Delta_h = 200$ , but the exact choice does not have a significant impact on our results.

In Fig. 1, we show the fraction of cosmic mass contained in haloes more massive than  $M_h$  as a function of  $M_h$ . Note that the mass functions given by the two simulations are similar except at the massive end where the small-box simulation gives a significantly lower fraction. This is largely due to the box-size effect. For comparison, we also plot the predictions based on the Press-Schechter mass function (Press & Schechter 1974) and the mass function of Sheth, Mo & Tormen (2001). As one can see, about 50% of the cosmic mass is contained in haloes with masses larger than  $10^{11} h^{-1} M_\odot$ , and about 40% is in haloes more massive than  $10^{12} h^{-1} M_\odot$ , in the CDM model considered here. If the normalization,  $\sigma_8$ , has a lower value, as may be the case according to the recent WMAP3 data (e.g. Spergel et al. 2007), these fractions are even lower. As shown in Yang et al. (2007), current large redshift surveys, such as the SDSS, can be used to select galaxy groups with masses down to  $10^{12} h^{-1} M_\odot$ . Thus, more than  $\sim 60\%$  of the cosmic mass is not directly associated with the virialized haloes of the galaxy groups that can be reliably identified from current redshift surveys. It is therefore

very important to investigate whether the mass component that is *not* directly observable can be reconstructed based on what we can see.

### 3 QUANTIFYING THE MASS DISTRIBUTION IN AND AROUND DARK MATTER HALOES

#### 3.1 The partitioning of the mass distribution

The goal of this paper is to use the distribution of dark matter haloes to reconstruct the cosmic density field. Since observationally we can only identify haloes above some mass threshold, the method is useful only if such reconstruction is based on haloes massive enough to be observationally identifiable. For a given mass threshold  $M_{\text{th}}$ , we refer all haloes with masses above it as the halo population. The cosmic mass (dark matter particles) in the universe can then be divided into two parts: (i) the halo component, which contains all the particles that are assigned to the proper of haloes above the mass threshold; (ii) the complementary component, which contains particles that are not assigned to the proper of these haloes. Note that some of the particles in the complementary component are in haloes of lower masses, while some may be in a diffuse form. As an illustration, we show in Fig. 2 the total mass distribution in a slice of the L300 simulation, along with the distributions of the halo and complementary components, assuming  $M_{\text{th}} = 10^{12} h^{-1} M_{\odot}$ . Clearly, the large-scale structure is well traced by the halo component, and the complementary component is tightly correlated with the halo component. Therefore, it is hopeful to use the halo component to reconstruct the full density field.

For a given halo population, we can partition space into a set of domains, each of which contains one halo. The domain of any halo is defined in such a way that each point in the domain is closer (based on a distance measure to be defined below) to the halo than to any other haloes in the halo population. With a proper definition of distance measure, each volume element (and each mass particle) can be assigned uniquely to a domain. The particles in the domain of a halo will be referred to as the domain particles of the halo.

We use the following quantity to describe the proximity of a point to a halo of virial radius  $R_h$ :

$$r_d = \frac{r_h}{R_h}, \quad (2)$$

where  $r_h$  is the physical distance between the halo center and the point. As an illustration,

Fig. 3 shows the domains of 10 randomly distributed haloes. Note that some small haloes and their domains are embedded in the domains of larger haloes. In this way, each particle in the complementary component is assigned to a unique domain. In the next section, we will discuss why we choose to use  $r_d = r/R_h$  to define domains.

### 3.2 Mass distribution in and around haloes

In order to reconstruct the cosmic density field accurately, we need to model the mass distribution in and around dark matter haloes. Here we use the cross-correlation function between the haloes and the mass in their domains to characterize the relation between the haloes and the surrounding mass distribution. This is different from the conventional cross-correlation function, which is defined by the mass density within spherical shells of a given radius centered on a halo, regardless whether or not the particles are in the domain of the halo. The advantage of our definition is that each particle (mass element) contributes only to the cross-correlation with one dark matter halo, thus avoiding the problem of double-counting when we use these profiles to reconstruct the density field. This turns out to be an important advantage. For instance, in the conventional definition, if we use the cross-correlation function as the average density profile around a halo to reconstruct the density field, then the reconstructed field will contain more mass than the original field, which has to be corrected for. However, it is not straightforward to rescale the density field while preserving the density fluctuations on small scales. With our domain-based definition of the cross correlation function, however, mass conservation is guaranteed by construction.

Since we want to obtain the correlation between the haloes and their corresponding domain particles, we modify the definition of the cross-correlation function as follows. First, for a given halo and a given spherical shell (with radius between  $r - \delta r/2$  and  $r + \delta r/2$  in unit of virial radius) centered on it, we calculate the volume of the intersection between its domain and the spherical shell [which we denote by  $V_h(r)$ ] as

$$V_h(r) = \sum_{p=1}^{N_h^p(r)} V_p, \quad (3)$$

where  $N_h^p(r)$  is the number of domain particles within the shell and  $V_p$  is the effective volume of the Delaunay tessellations associated with a domain particle  $p$ . Direct calculation of the intersection volume is very time consuming. This is the reason why we use instead the estimate given by equation (3) (see Appendix A for details). Our test based on a subset of haloes showed that this estimate is sufficiently accurate for the calculation of the cross

correlation function. Thus, for a set of  $N_h$  haloes, the total volume of such intersections can be obtained by summing up  $V_h(r)$  over all the haloes. We denote this volume by  $V_s(r)$ .

Finally, the average density profile can be estimated from

$$\bar{\rho}(r) = \frac{\sum_{h=1}^{N_h} \sum_{p=1}^{N_h^p(r)} M_p}{V_s(r)} = \frac{\sum_{h=1}^{N_h} N_h^p(r) M_p}{\sum_{h=1}^{N_h} \sum_{p=1}^{N_h^p(r)} V_p}, \quad (4)$$

where  $M_p$  is the mass of a particle. As mentioned above, this average density profile is different from that based on the conventional cross correlation function between haloes and mass, because here the number of halo-particle pairs is estimated only between a halo and its domain particles. In Fig. 4 we show the averaged density profiles for haloes in 6 mass bins, using  $M_{\text{th}} = 1.68 \times 10^{11} h^{-1} M_{\odot}$ . Note that the mass resolution of the L300 simulation is insufficient to resolve small halos, and it is used only to derive the density profiles in the domain associated with halos above  $10^{13} h^{-1} M_{\odot}$ , which contain at least 590 particles. For smaller halos, the profiles are obtained from L100. The boxsize of L100 may be too small to represent a real survey, but should be reliable for estimating the profiles around halos. Note also that, since the purpose of the paper is to test the reconstruction method, rather than probing the model prediction, the inaccuracy of the simulation should not have significant impact on our reconstruction which involves other more serious uncertainties (see below).

For comparison, the corresponding results using  $M_{\text{th}} = 10^{12} h^{-1} M_{\odot}$  and  $M_{\text{th}} = 10^{12.5} h^{-1} M_{\odot}$  are plotted in Figs. 5 and 6, respectively. As shown in Yang et al. (2005; 2007), the values  $M_{\text{th}} = 10^{12} h^{-1} M_{\odot}$  ( $3.16 \times 10^{12} h^{-1} M_{\odot}$ ) represent the lower-mass limit to which a complete group sample can be selected from the SDSS galaxy catalogue to a redshift of  $z \sim 0.1$  (0.15). The density profiles within the virial radius are well fitted by NFW profiles (Navarro et al. 1997), and the resulting concentration-mass relation is in a good agreement with that obtained by, e.g. Bullock et al. (2001). Here we do not take into account the scatter in the concentration-mass relation, because it is difficult to obtain the concentrations of individual systems from observation and it is important to examine how the lack of such information affects the reconstruction results. At radii larger than  $R_h$ , the profiles we obtain are comparable to what Prada et al. (2006) obtained for isolated haloes. As one can see, the density profile is measured over the range from  $0.05 R_h$  to about  $30 R_h$ , or in terms of density, from  $\sim 4 \times 10^4 \rho_m$  to  $\sim 0.1 \rho_m$ . These demonstrate that, for a given cosmology, current computer simulations can be used to determine reliably the cross-correlation functions to be used in our reconstruction model. The average density profile around  $(2 \rightarrow 3)R_h$  decreases slightly with increasing halo mass, mainly because the effect of infall increases with halo mass (e.g.



Prada et al. 2006). The density profile at large scales is higher for a higher mass threshold, because a large fraction of the cosmic mass is assigned to the complementary component.

In what follows, we will use these density profiles and halo/domain information to make the reconstruction. The choice of the definition of  $r_d$  is only useful if the derived profiles as function of  $r_d$  depend only weakly on halo mass so that the reconstructed density has no jump at the boundary of the domains. The cross correlation within the virial radius has the same form as the NFW profile, which depends only weakly on halo mass when the radius is scaled with the halo virial radius. As shown in Figs.4 – 6, the density profiles outside the virial radius also depend weakly on halo mass, indicating the usefulness of using  $r_d$  to represent radius.

## 4 RECONSTRUCTING THE COSMIC DENSITY FIELD

As we have mentioned in the introduction, our reconstruction method is based on the assumption that the density field is similar to that predicted by the current  $\Lambda$ CDM model, and we have shown in the previous section that the density profiles in and around dark matter haloes, which are required in our reconstruction model to be described below, can be estimated reliably from current numerical simulations. In this section we will describe how to reconstruct the dark matter distribution based on the distribution of dark haloes. We will first introduce our method and do the reconstruction based on the halo population in simulation L300, although the density profiles are from both L300 and L100. Then we compare our results with the original simulation, i.e. L300, by using several methods.

It should be pointed out that, although our reconstruction is based on the two-point correlation function between haloes and the mass density field, it contains high-order information through the inclusion of the halo-halo correlation, and of some environmental information, such as that represented by the domains.

### 4.1 The Reconstruction Method

Our reconstruction scheme consists of the following steps.

- We start with a sample of dark matter haloes above a mass threshold,  $M_{\text{th}}$ , each of which has a mass and a position in space.
- For a halo  $h$  we pick the average density profile for all haloes in a given mass bin that includes the mass of the halo in question.

- We use a Monte-Carlo method to put particles around the halo  $h$  up to  $\sim 30$  times virial radius (sufficient to cover the domain of the halo) regardless of the domain, using the density profile picked above. The mass of each of the sampling particles is exactly the same as the particle mass in the simulation L300. For convenience, we use  $S_h$  to denote this set of sampling particles.

- For each particle in  $S_h$ , we check whether the distance  $r_d$  [defined in equation (2)] between the particle and the center of halo  $h$  is smaller than that to any other haloes in the halo population. If yes, the particle is retained; otherwise it is removed. Thus, only particles in the domain of halo  $h$  are retained.

- Repeating the Steps 2, 3, and 4 for all haloes in the halo population, we obtain a reconstructed density field sampled by particles. Because of the way our cross-correlation function between haloes and domain particles are defined, the reconstructed density field has a total mass that is very similar to the original field.

On large scales, our reconstruction method ensures that the density field is the same as that traced by the distribution of the halo population. On small scales, our method reproduces the cross-correlation between haloes and dark matter. The idea behind our method is very similar to that in the current halo model (e.g. Jing et al. 1998; Cooray & Sheth 2002 and references therein), which models the mass distribution by convolving the distribution of dark matter haloes with their density profiles. The difference is that, while the halo model is based on all haloes and their density profiles within the virial radii, our model is based on relatively high mass haloes and the distribution of the complementary mass component around these haloes. Our approach is more useful in reconstructing the cosmic mass density field from observations, because redshift surveys can only be used to identify relatively massive haloes, as described above.

## 4.2 The reconstructed versus the original density fields

To compare our reconstructed density field with the original density field, we use the SPH method (Monaghan 1992) to smooth the reconstructed and simulated particle distributions on a Cartesian grid with grid-sizes of  $l_b = 250 h^{-1} \text{kpc}$  (see Appendix B for the detail). In what follows, we refer to this grid as our ‘base-grid’. In order to investigate the accuracy of our reconstruction method, we compare the reconstructed density field  $\rho_{\text{rec}}$  and the original

density field  $\rho_{\text{sim}}$  by applying different smoothing methods and smoothing scales on the density field on the base-grid.

The top-left panels of Fig. 7, 8 and 9 show the comparison in which the mass distributions on our base-grid are box-car smoothed on a scale of  $l_{\text{sm}} = 1 h^{-1}\text{Mpc}$  for three different reconstructions with halo mass thresholds of  $1.68 \times 10^{11}$ ,  $10^{12}$  and  $10^{12.5} h^{-1}\text{M}_{\odot}$ , respectively. Note that the smoothed density is simply computed by averaging over the enclosed base-grid cells, which in the case of  $l_{\text{sm}} = 1 h^{-1}\text{Mpc}$  corresponds to  $28^3$  grid-cells. The solid line represents the mean relation, while the error bars indicate the standard deviation in  $\rho_{\text{sim}}$  for given  $\rho_{\text{rec}}$ . As one can see, the bias in the mean relation is very small. However, in the low-density regime the scatter is quite large, especially for reconstructions with large  $M_{\text{th}}$ . This is expected, because the density field in the low-density regions is not sampled in detail by the population of massive haloes. In order to suppress these fluctuations, one may smooth the density field on even larger scales. In the middle-left and bottom-left panels, we show results using  $l_{\text{sm}} = 2 h^{-1}\text{Mpc}$  and  $4 h^{-1}\text{Mpc}$ , respectively. As expected, the scatter in the low density bins is now reduced.

Unfortunately, the use of a large smoothing length dilutes the high-density regions, thus reducing the dynamical range probed. As a compromise, we therefore introduce an adaptive smoothing length  $l_{\text{ad}}(M_{\text{s}}) = n l_{\text{b}}$  to smooth the density field, where  $M_{\text{s}}$  is a chosen smoothing mass scale (hereafter referred to as SMS), and  $n$  is an adjustable, even integer. The value of  $n$  is tuned so that the mass contained in the super-grid of  $l_{\text{ad}}(M_{\text{s}})$  first reaches  $M_{\text{s}}$ . In the right panels of Fig. 7, 8 and 9, we show the comparison between the reconstruction and simulation using  $M_{\text{s}} = M_{\text{th}}/2$ ,  $M_{\text{th}}$  and  $2M_{\text{th}}$  from top to bottom. Note that it is possible that at a given location the value of  $l_{\text{ad}}(M_{\text{s}})$  obtained from the reconstructed density field is different from that obtained from the original density field in the simulation. The adaptive smoothing length used above is based on the reconstructed field. By using  $M_{\text{s}} = 1 \sim 2M_{\text{th}}$ , our method reliably reconstructs the density field over a very large density range, because the small structures represented by halos with masses below  $M_{\text{th}}$ , which cannot be recovered by our method, is effectively smoothed. The large scatter in the intermediate density bins,  $\sim 20\rho_{\text{m}}$ , in the top-right panel of Fig. 7 ( $M_{\text{th}} = 1.68 \times 10^{11} h^{-1}\text{M}_{\odot}$ ,  $M_{\text{s}} = M_{\text{th}}/2$ ) is probably due to the neglect of substructures, especially large subhalos, in dark matter halos. Another reason is the definition of FOF halos, which suffer from the halo bridging problem (Tinker et al. 2008, Lukic et al. 2008). However, as discussed in Section 4.4, the use of elliptical model,

which takes care of the ‘bridging’ problem to some degree, does not make a significant improvement. Our test using spherical overdensity halos did not make significant difference.

As an illustration of the quality of our reconstruction, Fig. 10 shows the contours of the projected density distribution in a slice  $120 \times 120 \times 10 (h^{-1}\text{Mpc})$  of the reconstructed field (middle panels) in comparison with those obtained from the original density field (left panels). The different rows show contours at different levels. The mass threshold adopted here is  $M_{\text{th}} = 10^{12} h^{-1}M_{\odot}$ , and the density fields are smoothed on a scale of  $l_{\text{sm}} = 4 h^{-1}\text{Mpc}$ . As one can see, the reconstructed density field shows filamentary structure connecting high density nodes, similar to that in the original field. This is similar to the quantitative comparisons shown presented above.

We have also computed the power spectrum of the original and reconstructed density fields, using a Fast Fourier Transform of the overdensity on a  $1024^3$  grid (corresponding to an effective smoothing scale of  $l_{\text{sm}} \sim 300 h^{-1}\text{kpc}$ ). The overdensity is obtained using the Cloud-In-Cell (CIC) weighting scheme (Hockney & Eastwood 1981). The resulting power spectra are shown in the top panel of Fig 11 in comparison with that obtained directly from the simulation data (solid line). The bottom panel shows the difference between the reconstructed and original power spectra as a function of wave number  $k$ . The reconstruction results match the simulation very well on large scale. The fractional difference at  $k < 3 h\text{Mpc}^{-1}$  is less than 14% for all the reconstructions. The discrepancy is believed to be generated by the inaccuracy of our simple model for the mass distribution. For example, the underestimation on small scales ( $k > 3 h\text{Mpc}^{-1}$ ) is almost certainly due to the neglect of the structure in the complementary component produced by low mass haloes, the neglect of the substructure in massive haloes, and the bridging effect in FOF halos.

### 4.3 The predicted versus the original velocity fields

Since our final goal is to apply our method to observational data in redshift space, we have to deal with redshift space distortions due to the peculiar velocities of dark matter haloes. It is known that the large-scale peculiar velocity field is strongly correlated with the gravitational acceleration field (e.g. Colombi et al. 2007), and so it may be possible to predict the current velocity field using the current density field. If this is the case, we can then start with a density field in the redshift space, make corrections to the peculiar velocities, and iterate to get the real-space density distribution. In this subsection, we study how the reconstructed

density field can be used to make predictions for the peculiar velocities of haloes. In the next section, we will show how one can use this information in our reconstruction in order to account for redshift space distortions.

In the linear regime, the peculiar velocity is related to the density perturbation as

$$\mathbf{v}(\mathbf{k}) = Hf(\Omega)\frac{i\mathbf{k}}{k^2}\delta_{\mathbf{k}}, \quad (5)$$

where  $\mathbf{v}(\mathbf{k})$  and  $\delta_{\mathbf{k}}$  are the Fourier transforms of the velocity field and mass density contrast, respectively,  $H$  is the Hubble constant and  $f(\Omega) = \Omega_{\text{m}}^{0.6} + \Omega_{\Lambda}/70(1 + \Omega_{\text{m}}/2)$  (e.g. Lahav et al. 1991). Note that we are estimating the peculiar velocities of virialized haloes, for which the linear model is expected to yield a reasonable approximation. Since our reconstruction method is halo-based, the (strongly non-linear) virial motions within dark matter haloes are irrelevant.

We use the CIC scheme to construct the density field, on a  $1024^3$  grid, from the particles representing the reconstructed density field. Because the sizes of different haloes are different, we divide the halo population into 6 subsamples according to their masses. For a given subsample of haloes we use top-hat windows with radius equal to the average Lagrangian radius of the haloes in the sample to smooth the density field. We then use Fourier transform to obtain  $\delta_{\mathbf{k}}$ , and use equation (5) to obtain the linear velocity field. We use the linear velocity predicted at the position of a halo to represent the predicted velocity of the corresponding halo. In Fig. 12 we show the  $x$ -component of the predicted velocity versus that of the true velocity, using  $M_{\text{th}} = 10^{12} h^{-1} M_{\odot}$ . Overall, the predicted velocity is tightly correlated with the true velocity. For a very small fraction of haloes, the predicted velocity is significantly larger than the true one. These haloes are usually close to massive haloes, so that non-linear effects cannot be neglected, rendering Equation (5) inaccurate.

The dashed line in Fig. 13 shows the probability distribution of the difference between the predicted velocity based on the reconstruction and the true velocity. For comparison, the solid lines shows the same distribution but obtained using the simulated mass distribution. The two distributions are very similar, indicating that most of the error in the peculiar velocities is not due to errors in the reconstructed density field, but due to the limited applicability of linear theory. Our result is similar to that of Lavaux (2008), who used the Monge-Ampere-Kantorovitch method to infer the peculiar velocities of haloes and galaxies.

#### 4.4 Spherical versus Elliptical Model

So far we have used the spherically averaged cross-correlation between haloes and the mass in their domains to reconstruct the density field. However, haloes that form in the cosmological density field are generally ellipsoidal and should be modelled with a sequence of concentric triaxial distributions (e.g. Jing & Suto 2002). The non-spherical properties are expected to be even more prominent in the complementary component, where the mass distribution clearly shows filamentary and sheet-like structure (Fig. 2). In order to take such aspherical properties into account, we have attempted to model the density distribution in and around haloes using a two-dimensional profile. A crucial step here is to define the orientation of the local mass distribution. As shown in Hahn et al. (2007b), the major axes of dark matter haloes are strongly correlated with the local tidal field. Our own test using only the mass contained in the halo population confirms their results. This allows us to estimate two-dimensional profiles relative to the local tidal axes. We found that the cross-correlation function becomes increasingly elongated up to a scale about 5 times the halo virial radius, suggesting that the density field around haloes is indeed quite anisotropic. We have tried to use the two-dimensional profiles in our reconstruction, and found that the improvement over the spherical model is only very modest. There are several reasons for this. First of all, to first order, the large-scale filamentary and sheet-like structure has already been taken into account as long as  $M_{\text{th}} < M_{\star}^1$ . This owes to the fact that haloes with  $M_{\text{th}} < M_{\star}$  actually populate the filaments and sheets that connect the more massive haloes with  $M > M_{\star}$  (see Fig. 2). Second, the correlation between the major axes of the local mass distribution and the local tidal field is not perfect, especially for low-mass haloes, which compromises the accuracy of the model. Finally, comparing Figs. 7, 8 and 9 one sees that a large part of the discrepancy between the original field and the reconstruction on small scales is due to the lack of small scale structure corresponding to haloes with masses below  $M_{\text{th}}$ , which cannot be corrected for even with the two-dimensional model. Because the two-dimensional model is much more complicated to implement, and because the improvement it makes to the reconstruction is not substantial, we will only use the spherical model.

<sup>1</sup>  $M_{\star}$  is the characteristic mass scale at which the *RMS* of the linear density field is equal to 1.686 at the present time (for our  $\Lambda$ CDM cosmology  $M_{\star} \approx 1.0 \times 10^{13} h^{-1} M_{\odot}$ )

## 5 PERFORMANCE IN REDSHIFT SPACE

So far we have demonstrated that our reconstruction method works well in real space. Unfortunately, in real observations the positions of dark haloes represented by galaxy systems are only available in redshift space. In this section we examine how our method performs for a sample of haloes (groups) in redshift space. As a demonstration, here we focus on the case with  $M_{\text{th}} = 10^{12} h^{-1} M_{\odot}$ . In principle, we can start with the distribution of haloes in the redshift space, reconstruct a density field from this distribution, predict the peculiar velocities of haloes using the reconstructed density field, make corrections to the positions of haloes, and iterate until a convergence is achieved. Unfortunately, this procedure is very time-consuming, because we have to do the reconstruction in each iteration. Here we adopt a simplified method, using the fact that the distribution of dark matter haloes can be used to estimate the velocity field. It is well known that there is bias between the halo distribution and the cosmic mass distribution, and so the predicted velocity field based on the density distribution of haloes,  $\mathbf{v}_h$ , is biased with respect to the real velocity field. Fortunately, as shown in Colombi et al. (2007),  $\mathbf{v}_h$  is very tightly correlated with and directly proportional to the real velocity field. Using the linear model given in equation (5), we can write

$$\mathbf{v}_h(\mathbf{k}) = Hf(\Omega) \frac{i\mathbf{k}}{k^2} \delta_{\mathbf{k}}^h = bHf(\Omega) \frac{i\mathbf{k}}{k^2} \delta_{\mathbf{k}} = b\mathbf{v}(\mathbf{k}), \quad (6)$$

where  $\delta_{\mathbf{k}}^h$  is the Fourier transform of the mass density contrast represented by the mass contained in dark matter haloes, and  $b$  is a constant bias factor. In order to estimate the value of  $b$ , we assign the mass of haloes on grids in real-space to obtain  $\delta^h$  and use equation (6) to obtain the velocities,  $\mathbf{v}_h$ , for all haloes. Comparing  $\mathbf{v}_h$  with  $\mathbf{v}$  based on the original simulation we obtain  $b \sim 1.56$  for  $M_{\text{th}} = 10^{12} h^{-1} M_{\odot}$ . We have tried various smoothing mass scale (SMS) to see if the value of  $b$  is sensitive to the SMS. We found that the value of  $b$  is independent of the SMS. Fig. 14 shows  $\mathbf{v}$  versus  $\mathbf{v}_h/b$  for haloes of different masses, assuming a SMS of  $10^{14.75} h^{-1} M_{\odot}$  (this SMS turns out to be the best choice for correcting the redshift distortion, as we will see below). The two velocities are very tightly correlated, suggesting that the distribution of haloes can be used to predict the velocity field quite reliably.

From equation (6), one can see that the bias parameter  $b$  is actually the bias of the mass distribution in halos more massive  $M_{\text{th}}$  relative to the underlying mass distribution. Thus, we can write  $\delta^h = b\delta$ , so that

$$\xi_{\text{M,m}}(r, > M_{\text{th}}) = b\xi_{\text{m,m}}(r), \quad (7)$$

where  $\delta^h$  and  $\delta$  are the large-scale density perturbation represented by the mass within the halo population and the total mass, respectively;  $\xi_{M,m}(r, > M_{\text{th}})$  is the cross-correlation between the halo mass and the underlying mass, and  $\xi_{m,m}(r)$  is the autocorrelation of mass in the universe. It is then easy to show that, on large scale,  $\xi_{M,m}(r, > M_{\text{th}})$  is the sum of the halo-mass cross-correlation,  $\xi_{h,m}(r, M_h)$ , weighted by the halos mass:

$$\xi_{M,m}(r, > M_{\text{th}}) = \frac{\int_{M_{\text{th}}}^{\infty} \xi_{h,m}(r, M_h) M_h f(M_h) dM_h}{\int_{M_{\text{th}}}^{\infty} M_h f(M_h) dM_h}, \quad (8)$$

where  $M_h f(M_h) dM_h$  is the total mass in halos with masses in the bin  $[M_h, M_h + dM_h]$ . Mo & White (1996) showed that  $\xi_{h,m}(r, M_h)$  is approximately parallel to  $\xi_{m,m}(r)$  on large scale:

$$\xi_{h,m}(r, M_h) = b_h(M_h) \xi_{m,m}(r), \quad (9)$$

where  $b_h(M_h)$  is the bias parameter for halos of mass  $M_h$  (e.g. Mo & White 1996; Jing 1998; Sheth, Mo & Tormen 2001). Combining the equation 7 and 8, we obtain,

$$b = \frac{\int_{M_{\text{th}}}^{\infty} b_h(M_h) M_h f(M_h) dM_h}{\int_{M_{\text{th}}}^{\infty} M_h f(M_h) dM_h}. \quad (10)$$

Obviously, the bias  $b$  depends on  $M_{\text{th}}$  and the cosmology in question. In Fig. 15 we show the the value of  $b$  as a function of  $M_{\text{th}}$  predicted by the spherical collapse model (Mo & White 1996) and the elliptical collapse model (Sheth, Mo & Tormen 2001). For comparison, we also show the results obtained directly from the simulation. As one can see, the model predictions are in good agreement with the simulation results, suggesting that the value of  $b$  used in our reconstruction can also be estimated from the analytical models.

In the simulation, we choose the redshift direction to be along the  $x$ -axis of the simulation box. We first use the halo population in redshift space to compute the velocities,  $\mathbf{v}_h$ , and then use  $\mathbf{v} = \mathbf{v}_h/b$  as the prediction of the peculiar velocities of haloes to correct the positions of haloes. We iterate until convergence is achieved. However, as shown in Fig. 12, the velocities of haloes in general consist of two components, the linear velocities induced by large scale structures and the non-linear velocities induced by small-scale structures. Although the former can be easily corrected using linear theory, the nonlinear effect cannot be easily corrected, and so it is not very meaningful to compare the reconstructed field and the original field on small scales. Because of this, we set a minimal SMS,  $M_{\text{min}}$  and use the larger of  $M_h$  and  $M_{\text{min}}$  as the SMS for a halo of mass  $M_h$ . In order to choose the value of  $M_{\text{min}}$ , we define the following parameter to quantify the quality of the correction for the redshift distortion:



$$A_d = \frac{\sum_{h=1}^N M_h |\mathbf{x}_h^o - \mathbf{x}_h^p|}{\sum_{h=1}^N M_h}, \quad (11)$$

where  $\mathbf{x}_h^o$  and  $\mathbf{x}_h^p$  are the original and predicted positions of halo  $h$ . Thus,  $A_d$  is the average, mass-weighted offset between the original and predicted halo positions. We found that, for the total sample of haloes,  $A_d$  is minimized when  $M_{\min}$  is about  $10^{14.75} h^{-1} M_\odot$ . The value of  $A_d$  at the minimum is about  $1.2 h^{-1} \text{Mpc}$ . We also find that the values of  $M_{\min}$  required for haloes of different masses are quite similar. Notice that  $1.2 h^{-1} \text{Mpc}$  corresponds to  $120 \text{km/s}$ , which is similar to the typical error in the predicted peculiar velocities of dark matter haloes shown in Fig. 12. Because of this, we choose  $M_{\min} = 10^{14.75} h^{-1} M_\odot$  to estimate the peculiar velocities and correct for the redshift distortion.

With the corrected halo positions described above, we use the same method as described in Section 4 to reconstruct the density field. The right three panels of Fig. 10 give a visual impression of the density field thus obtained. As one can see, the large scale structure is well recovered. The corresponding power spectrum is shown in the top panel of Fig. 11, and is almost indistinguishable from that obtained from the real-space reconstruction. In Fig. 16 we show the reconstructed field in comparison to the original density field. As expected, the correlation between the reconstruction and simulation is worse than that based on the halo population in real space, because of the offset between the predicted halo positions and the corresponding real positions. However, using a relatively large smoothing length,  $l_{\text{sm}} \geq 5 h^{-1} \text{Mpc}$ , the scatter is within a factor of 2. Here, we do not use the adaptive smoothing method, because the sizes of the high-density regions, i.e. the inner regions of the halos, are smaller than the typical offset of the halo positions.

We have also estimated the peculiar velocities of haloes based on the reconstructed field using redshift-space data. The comparison with the true velocities is shown in Fig. 17. The predicted velocities are computed using the method described in Section 4.3. For most haloes, the predicted velocities are tightly correlated with the true velocities, but for a small fraction of haloes the difference is quite large. This is also demonstrated in Fig. 13, where we show the distribution of the difference between the predicted and true velocities. As one can see, compared with the result obtained from the real-space data, the distribution obtained with the redshift-space data has extended tails. However, the fraction of systems in the tails is relatively small: only about 25% of the systems have a velocity difference larger than  $200 \text{km s}^{-1}$ . There are two kinds of effects which can produce such discrepancy: one owes to the reconstruction, the other is the mismatch of the halo positions. In order

to investigate which plays a dominant role, we performed the following test. We use the reconstruction in **redshift**-space to calculate the velocity field and then use the velocities at the positions of the haloes in **real**-space as the test velocities. The dot-dashed line in Fig. 13 shows the probability distribution of the difference between these test velocities and the true halo velocities. Note that the extended tails have now disappeared, indicating that the tails owe mainly to the mismatch of the halo positions.

Finally, we use the density field reconstructed from the redshift-space data to compute the large tidal field, which may play an important role in the formation of dark matter haloes and galaxies (e.g. Hahn et al. 2007a,b; Wang, Mo & Jing 2007). We first use CIC scheme to generate the density field on  $1024^3$  grids and then smooth it using a Gaussian kernel. Following Hahn et al. (2007a), we set our SMS equal to  $2M_*$ . We use the Fast Fourier Transform to solve the Poisson equation and apply the second derivative operator to obtain the tidal tensors. We compute the eigenvalues  $\lambda'_1, \lambda'_2, \lambda'_3$  ( $\lambda'_1 \geq \lambda'_2 \geq \lambda'_3$ ), and the corresponding eigenvectors  $\mathbf{d}'_1, \mathbf{d}'_2, \mathbf{d}'_3$  of the tidal tensor at the predicted position of each halo. In order to examine whether our reconstruction can recover the true tidal field, we compare the eigenvalues and eigenvectors obtained from the reconstructed field based on redshift-space data with those obtained from the original simulation,  $\lambda_1, \lambda_2, \lambda_3$  and  $\mathbf{d}_1, \mathbf{d}_2, \mathbf{d}_3$  in Fig. 18. In the left three panels we show the distribution of the dot product  $\mu_{ii}$  between  $\mathbf{d}'_i$  and  $\mathbf{d}_i$  ( $i = 1, 2, 3$ ). As one can see, the reconstructed  $\mathbf{d}'_i$ s are strongly aligned with the corresponding true  $\mathbf{d}_i$ s. The values of  $\lambda'_i$ s are also strongly correlated with  $\lambda_i$ s, as shown in the three middle panels of Fig. 18. To quantify the correlation, we define a parameter  $\beta_i = |\lambda'_i - \lambda_i|/|\lambda_i|$ , and show the distribution of  $\beta_i$ s in the three right panels. The values of  $\beta_i$  are quite small for the majority of the haloes. Note that, on average,  $\beta_{11} < \beta_{33} < \beta_{22}$ ; this simply owes to the fact that  $|\lambda_1| > |\lambda_3| > |\lambda_2|$  on average.

## 6 DISCUSSION

In this paper, we have used  $N$ -body simulations to demonstrate the promise of using the distribution of dark matter haloes to reconstruct the underlying density field. This paper serves only as a proof of concept, and the applications of the method to real data will be presented in forthcoming papers. In this discussion section, we outline some of the questions that can be addressed with a well-reconstructed cosmic density field.

The largest redshift sample of galaxies now available is that given by the SDSS. With the

SDSS group (halo) catalogue constructed by Yang et al. (2007), it is in principle straightforward to apply the reconstruction procedures described above to obtain the current density field in the SDSS volume. Since the observed positions of haloes are in redshift space, one has to take into account redshift distortion. As discussed above, the structures traced by dark matter haloes are expected to be in the mildly non-linear regime, and so a correction for peculiar velocities can be made using the reconstructed mass distribution in an iterative way. In addition to redshift distortion, the observational group sample also suffers from incompleteness and contaminations due to observational selection effects and errors introduced by the group finder, from the uncertainties in the halo mass assignments to groups, and from the boundary effects. The results of several tests demonstrated that the method of halo-mass assignment is statistically reliable. Yang et al. (2007) tested the group finder using mock catalogs and found that the group finder successfully selects more than 90 percent of all the true halos in  $N$ -body simulations, and that the scatter between the estimated and true halo masses is about 0.3 dex. Yang et al. (2005) and Wang et al. (2008) estimated the clustering bias of halos as a function of group mass, and found very good agreement with the mass dependence of halos in  $N$ -body simulation, which is not expected if the halo masses assigned to galaxy groups are in serious error. Finally, in a recent investigation, Li et al. (2008) found that the group catalog selected from the SDSS, combined with the masses assigned to groups can reproduce the galaxy-galaxy weak lensing signal observed by Mandelbaum et al. (2006). Nevertheless, the impact of all the factors should be tested and quantified with the use of detailed mock catalogues, such as the ones presented in Yang et al. (2005; 2007). We will come back to this in a forthcoming paper.

Recent results from  $N$ -body simulations show that the formation history of a dark matter halo can be significantly affected by its large-scale environment (Gao et al. 2005; Wechsler et al. 2006; Wang et al. 2007; Jing, Suto & Mo 2007). Furthermore, the structure and kinematics of dark matter haloes, such as its shape and angular momentum, may also be correlated with the large-scale environments of haloes (e.g. Faltenbacher et al. 2007). Since galaxies form in dark matter haloes, the environmental dependence of halo properties is expected to produce observable correlations between galaxy properties and large-scale structure. Indeed, recent gas-dynamical simulations demonstrate that the accretion of cold gas into dark matter haloes to form galaxies is dominated by flows along filaments (Kereš et al. 2005). With our reconstructed density field, we will be able to define in detail the environments of all the galaxies in the SDSS based on their neighboring galaxies as well as on the tidal fields owing

to large scale structure. It is then straightforward to analyze how the properties of individual galaxies, such as shape, orientation, angular momentum, size, and gas content, are correlated with the large-scale environments. Some investigations along this line have been carried out successfully using different redshifts surveys and methods (e.g. Lee & Erdoğdu 2007; Longo 2007; Lee & Lee 2008).

A key step in understanding galaxy formation in the cosmic density field is to study the distribution, state and chemical composition of the diffuse gas, i.e. gas that has not been incorporated into galaxies, and its relationship to the galaxy population. There have been many observational programs dedicated to various aspects of this IGM component. Extensive X-ray observations have been conducted to study the hot gas associated with clusters and rich groups of galaxies but one expects the total mass associated with such systems to be small. As shown in Mo & White (2002), at the present time only  $\sim 10\%$  of the cosmic mass is in virialized haloes with virial temperatures above 1 KeV. About 70% of all the mass is in virialized haloes with virial temperatures below  $10^6$  K, too cold to be studied using X-ray observations. A more promising, and perhaps the only way, to study the bulk of the diffuse IGM is through absorption lines. The capability of this approach has been demonstrated very convincingly at high redshift, where observations of Lyman- $\alpha$  and metal absorption lines using optical spectroscopy have identified almost all of the baryonic component and have provided important clues about the nature of the IGM at  $z \sim 3$  (e.g. Rauch et al. 1998 and references therein). At low redshift ( $z \sim 0$ ), the situation is more complicated. First of all, one needs UV or X-ray spectroscopy, meaning space-based observations, to study the common atomic absorption lines. Secondly, at low- $z$  a larger fraction of the IGM may have been affected by gravitational collapse and non-gravitational processes, such as star formation and AGN activities. The structure, state and composition of the gas to be studied is, therefore, more complex making the interpretation of observational results more challenging. Observations with the *Far Ultraviolet Spectroscopic Explorer (FUSE)* and the *Hubble Space Telescope (HST)* and its *Space Telescope Imaging Spectrograph (STIS)* have demonstrated the promise of using UV absorption systems to identify the diffuse component of the IGM at low redshifts. These observations have so far revealed a wide array of absorptions lines, ranging from low ions such as HI all the way up to highly ionized species, such as OVI and NeVIII (e.g. Stocke et al. 2004; Tripp & Bowen 2005 and references therein), presumably associated with the warm-hot medium seen in gas-dynamical simulations (e.g. Cen & Ostriker 1999; Davé et al. 2001). With spectrographs aboard the *Chandra* and *XMM/Newton* X-ray

telescopes, it is now also possible to probe the IGM through very highly-ionized species, such as OVII, OVIII, and NeIX. The current sample is still too small to allow a systematic and detailed exploration of the IGM, but fortunately the situation is expected to improve soon with the installation of the *Cosmic Origins Spectrograph* (*COS*) on the *HST* and the launch of a future X-ray satellite, *X-ray Evolving-Universe Spectroscopy* (Kawahara et al. 2006); the sample of the absorption systems should increase by an order-of-magnitude or more. Clearly, it is important to examine in detail how such observations can be used to identify the missing component of the IGM at low- $z$  and to study its properties in a systematic way.

Absorption studies at low-redshift have suffered from a lack of suitable background sources, i.e. quasars and gamma-ray bursts, and from the difficulty in obtaining high-quality UV spectroscopy. It is, therefore, imperative to have as much theoretical and empirical input as possible both to design an optimal observational strategy and to help interpret the limited amount of observational data. With a detailed map of the local density field obtained from the reconstruction method described here, we can obtain detailed information about the environment in which the absorption occurs. This is particularly useful for interpreting the observational data of low- $z$  absorption systems, because here the sample is small and cosmic variance is a major concern. The uncertainties are minimized if comparisons between the observations and the model predictions are made for systems with the same large-scale environments.

## 7 SUMMARY

In this paper we have developed a method to reconstruct cosmic density field from the distribution of dark matter haloes above a certain mass threshold,  $M_{\text{th}}$ . Our method uses the fact that the statistical properties of the large-scale structure are well represented by the current  $\Lambda$ CDM model. In order to describe the distribution of the mass in and around dark matter haloes, each volume element in space is assigned to the domain of the nearest halo according to a distance measure that is scaled by the virial radius of the halo. The density profiles associated with dark matter haloes are then modelled using the cross-correlation function between dark matter haloes and the mass distribution within their domains. In this paper of proof-of-concept, we use two sets of high-resolution N-body simulation to calculate such profiles. Within the virial radii, these density profiles are well represented by the NFW profile, and on larger scales the profiles are comparable to those obtained by Prada et al.

(2006). These density profiles are used to sample the mass distribution in the domains of all haloes to reconstruct the density field that are not associated with the virialized haloes above the mass threshold. Since our reconstruction uses the distribution of dark matter haloes, it ensures that the reconstructed density field is the same as that traced by the halo population, and on small scales it reproduces the NFW profiles within individual haloes. We have considered three cases, using  $M_{\text{th}} = 1.68 \times 10^{11}$ ,  $10^{12}$  and  $10^{12.5} h^{-1} M_{\odot}$ , respectively. The later two values represent the lower-mass limit of complete group samples that can be selected from SDSS to a redshift of  $z \sim 0.1$  and  $0.15$ . Clearly, the density field is better reconstructed with a smaller  $M_{\text{th}}$ . A comparison between the reconstructed field and the original field shows that our method can reconstruct the density accurately, with an error typically of 50%, on mass scales comparable to or larger than  $(1 \rightarrow 2)M_{\text{th}}$ . The reconstructed density field can be used to estimate the peculiar velocities of dark matter haloes with a typical error of  $\sim 100 \text{ km s}^{-1}$ .

We also test the reliability of our method working in redshift space. To do this, we start with the positions of haloes in redshift space to estimate the peculiar velocities and use iterations until convergence is achieved. The positions of haloes in the final iteration are then used to do the reconstruction. Because of the error in the predicted peculiar velocities, there are offsets between the predicted positions of haloes and the real positions. This leads to mismatch between the reconstructed field and the original field on small scales. However, the density and velocity field on large scales are still well reconstructed.

We have outlined some potential applications of our reconstruction method. Our final goal is to apply this method to observational data, such as the SDSS group catalogue. With a well-reconstructed density field in the local universe, we can study in detail how the properties of galaxies are affected by their large-scale environments. Our reconstruction can also be used to study the correlation between the gas component to be revealed by QSO absorption systems at low-redshift with the large-scale environments.

## ACKNOWLEDGMENTS

We acknowledge the support from the Supercomputing Center of USTC. HYW would like to acknowledge the support of the Knowledge Innovation Program of the Chinese Academy of Sciences, Grant No. KJCX2-YW-T05 and NSFC 10643004. HJM would like to acknowledge the support of NSF AST-0607535, NASA AISR-126270 and NSF IIS-0611948. YPJ

is supported by NSFC (10533030), by the Knowledge Innovation Program of CAS (No. KJCX2-YW-T05), and by 973 Program (No.2007CB815402).

## REFERENCES

- Barber, C. B., Dobkin, D. P., & Huhdanpaa, H. T. (1996). The Quickhull algorithm for convex hulls. *ACM Trans. on Mathematical Software*, 22(4),469–483
- Bardeen J. M., Bond J. R., Kaiser N., Szalay A. S., 1986, *ApJ*, 304, 15
- Bartelmann M., Schneider P., 2001, *PhR*, 340, 291
- Berlind A. A., Weinberg D. H., 2002, *ApJ*, 575, 587
- Bullock J. S., Kolatt T. S., Sigad Y., Somerville R. S., Kravtsov A. V., Klypin A. A., Primack J. R., Dekel A., 2001, *MNRAS*, 321, 559
- Cen R., Ostriker J. P., 1999, *ApJ*, 514, 1
- Croton D. J., et al., 2006, *MNRAS*, 365, 11
- Cole S., Lacey C. G., Baugh C. M., Frenk C. S., 2000, *MNRAS*, 319, 168
- Colless M., et al., 2001, *MNRAS*, 328, 1039
- Colombi S., Chodorowski M. J., Teyssier R., 2007, *MNRAS*, 375, 348
- Cooray A., 2006, *MNRAS*, 365, 842
- Cooray A., Sheth R., 2002, *PhR*, 372, 1
- Davé R., et al., 2001, *ApJ*, 552, 473
- Erdođdu P., et al., 2004, *MNRAS*, 352, 939
- Evrard A. E., Metzler C. A., Navarro J. F., 1996, *ApJ*, 469, 494
- Faltenbacher A., Li C., Mao S., van den Bosch F. C., Yang X., Jing Y. P., Pasquali A., Mo H. J., 2007, *ApJ*, 662, L71
- Fisher K. B., Lahav O., Hoffman Y., Lynden-Bell D., Zaroubi S., 1995, *MNRAS*, 272, 885
- Gao L., Springel V., White S. D. M., 2005, *MNRAS*, 363, L66
- Gastaldello F., Buote D. A., Humphrey P. J., Zappacosta L., Bullock J. S., Brighenti F., Mathews W. G., 2007, *ApJ*, 669, 158
- Hahn O., Porciani C., Carollo C. M., Dekel A., 2007a, *MNRAS*, 375, 489
- Hahn O., Carollo C. M., Porciani C., Dekel A., 2007b, *MNRAS*, 381, 41
- Hockney R. W., Eastwood J. W., 1981, *csup.book*,
- Jing Y. P., 1998, *ApJ*, 503, L9
- Jing Y. P., Mo H. J., Boerner G., 1998, *ApJ*, 494, 1

- Jing Y. P., Suto Y., 2002, *ApJ*, 574, 538
- Jing Y. P., Suto Y., Mo H. J., 2007, *ApJ*, 657, 664
- Kang X., Jing Y. P., Mo H. J., Börner G., 2005, *ApJ*, 631, 21
- Kauffmann G., White S. D. M., Guiderdoni B., 1993, *MNRAS*, 264, 201
- Kauffmann G., White S. D. M., Heckman T. M., Ménard B., Brinchmann J., Charlot S., Tremonti C., Brinkmann J., 2004, *MNRAS*, 353, 713
- Katz N., Weinberg D. H., Hernquist L., 1996, *ApJS*, 105, 19
- Kawahara H., Yoshikawa K., Sasaki S., Suto Y., Kawai N., Mitsuda K., Ohashi T., Yamasaki N. Y., 2006, *PASJ*, 58, 657
- Kereš D., Katz N., Weinberg D. H., Davé R., 2005, *MNRAS*, 363, 2
- Lahav O., Lilje P. B., Primack J. R., Rees M. J., 1991, *MNRAS*, 251, 128
- Lavaux G., 2008, arXiv, 801, arXiv:0801.4208
- Lee J., Erdogdu P., 2007, *ApJ*, 671, 1248
- Lee J., Lee B., 2008, arXiv, 801, arXiv:0801.1558
- Li, R., Mo, H.J., Fan, Z., Cacciato, M., van den Bosch, F.C., Yang, X.H., More S., 2008, *MNRAS*, submitted
- Longo M. J., 2007, arXiv, 707, arXiv:0707.3793
- Lukić Z., Reed D., Habib S., Heitmann K., 2008, arXiv, 803, arXiv:0803.3624
- Mathis H., Lemson G., Springel V., Kauffmann G., White S. D. M., Eldar A., Dekel A., 2002, *MNRAS*, 333, 739
- Mo H. J., White S. D. M., 1996, *MNRAS*, 282, 347
- Mo H. J., White S. D. M., 2002, *MNRAS*, 336, 112
- Monaghan J. J., 1992, *ARA&A*, 30, 543
- Navarro J. F., Frenk C. S., White S. D. M., 1997, *ApJ*, 490, 493
- Peacock J. A., Smith R. E., 2000, *MNRAS*, 318, 1144
- Pearce F. R., Thomas P. A., Couchman H. M. P., Edge A. C., 2000, *MNRAS*, 317, 1029
- Prada F., Klypin A. A., Simonneau E., Betancort-Rijo J., Patiri S., Gottlöber S., Sanchez-Conde M. A., 2006, *ApJ*, 645, 1001
- Press W. H., Schechter P., 1974, *ApJ*, 187, 425
- Rauch M., 1998, *ARA&A*, 36, 267
- Schmoldt I. M., et al., 1999, *AJ*, 118, 1146
- Scranton R., 2003, *MNRAS*, 339, 410
- Sheth R. K., Mo H. J., Tormen G., 2001, *MNRAS*, 323, 1



- Somerville R. S., Primack J. R., 1999, MNRAS, 310, 1087
- Spergel, D. N., et al. 2007, ApJS, 170, 377
- Springel V., 2005, MNRAS, 364, 1105
- Springel V., et al., 2005, Natur, 435, 629
- Stoche J. T., Shull J. M., Penton S. V., 2004, astro, arXiv:astro-ph/0407352
- Tinker J. L, Kravtsov A. V, Klypin A., Abazajian K., Warren M. S, Yepes G., Gottlober S., Holz D. E, 2008, arXiv, 803, arXiv:0803.2706
- Tinker J. L., Weinberg D. H., Zheng Z., Zehavi I., 2005, ApJ, 631, 41
- Tripp T. M., Bowen D. V., 2005, pgqa.conf, 5
- Vale A., Ostriker J. P., 2006, MNRAS, 371, 1173
- van den Bosch F. C., 2002, MNRAS, 332, 456
- van den Bosch F. C., Yang X., Mo H. J., 2003, MNRAS, 340, 771
- van den Bosch F. C., et al., 2007, MNRAS, 376, 841
- Wang H. Y., Mo H. J., Jing Y. P., 2007, MNRAS, 375, 633
- Wang, Y., Yang, X.H., Mo, H. J., van den Bosch, F.C., Weinmann, S. M., Chu, Y., 2007, arXiv0711.4431
- Wechsler R. H., Zentner A. R., Bullock J. S., Kravtsov A. V., Allgood B., 2006, ApJ, 652, 71
- Weinmann S. M., van den Bosch F. C., Yang X., Mo H. J., 2006, MNRAS, 366, 2
- White S. D. M., Frenk C. S., 1991, ApJ, 379, 52
- White, S. D. M., & Rees, M. J. 1978, MNRAS, 183, 341
- Yan R., Madgwick D. S., White M., 2003, ApJ, 598, 848
- Yang X., Mo H. J., van den Bosch F. C., 2003, MNRAS, 339, 1057
- Yang X., Mo H. J., van den Bosch F. C., Jing Y. P., 2005, MNRAS, 356, 1293
- Yang X., Mo H. J., van den Bosch F. C., Pasquali A., Li C., Barden M., 2007, ApJ, 671, 153
- York D. G., et al., 2000, AJ, 120, 1579
- Zaroubi S., Hoffman Y., Fisher K. B., Lahav O., 1995, ApJ, 449, 446
- Zheng Z., et al., 2005, ApJ, 633, 791

**Appendix A:** Note on the effective volume

Delaunay Density Estimator Method was used by Schaap & van de Weygaert (2000, hereafter SW2000; see also Wang's phd thesis) to construct a continuous density field based on a sample of discrete data points and has been demonstrated to have optimal performance

in both high and low density regions than the conventional methods, such as the grid-based TSC method and the SPH smoothing kernel method. It *divides the space into a unique and volume-covering network of mutually disjunct Delaunay tetrahedra* (SW2000, see their figure 1) and the vertices of the tetrahedra are just the CDM particles. So the density at a vertex, e.g. at the position of particle ‘p’, is

$$\rho_p = \frac{4M_p}{W_{Vor,p}}. \quad (1)$$

According to this formula we define the effective volume of particle ‘p’ as

$$V_p = \frac{W_{Vor,p}}{4}, \quad (2)$$

where  $W_{Vor,p}$  is the sum of volume of all tetrahedra associated with this vertex. Obviously, the value of  $W_{Vor,p}$  is determined by the nearby particles distribution. The method is fully adaptive and follows the mass conservation and volume conservation (see SW2000 for more details).

We use the publicly released software Qhull<sup>2</sup> (Barber et al. 1996) to generate the Delaunay tetrahedra and use equation (2) to calculate the effective volume associated with each CDM particle.

### **Appendix B:** Note on the SPH smoothing method

Since the density gradient is very steep within the virial radius of halos, the density at the center of the ‘base-grid’, with a size of  $250 h^{-1} \text{kpc}$  on a side, cannot be used to represent the average density of the whole ‘base-grid’. In order to recover the density properly, we divide the ‘base-grid’ into  $7^3$  sub-grids, with the grid-size comparable to the softening length used in the simulation. Then we use SPH method to smoothing the particle distribution on the sub grid. The smoothing is performed using the  $N_{\text{sph}} = 32$  nearest neighbors to each sub-grid-point. We adopt the following SPH kernel (Monaghan 1992),

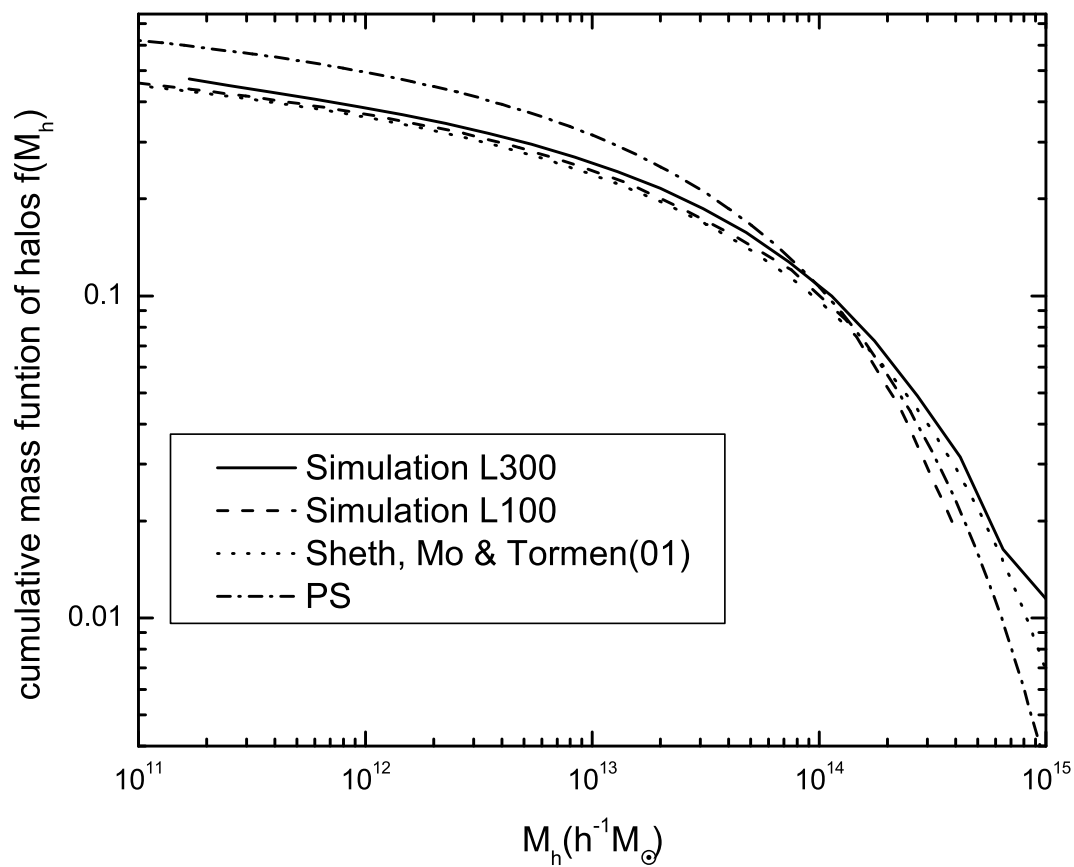
$$\zeta(x) = \begin{cases} 1 - 1.5x + 0.75x^3, & (0 \leq x \leq 1) \\ 0.25(2 - x)^2, & (1 \leq x \leq 2) \\ 0, & (x > 2) \end{cases},$$

and obtain the density  $\rho$  on a sub grid site,  $\mathbf{r}_g$ , using

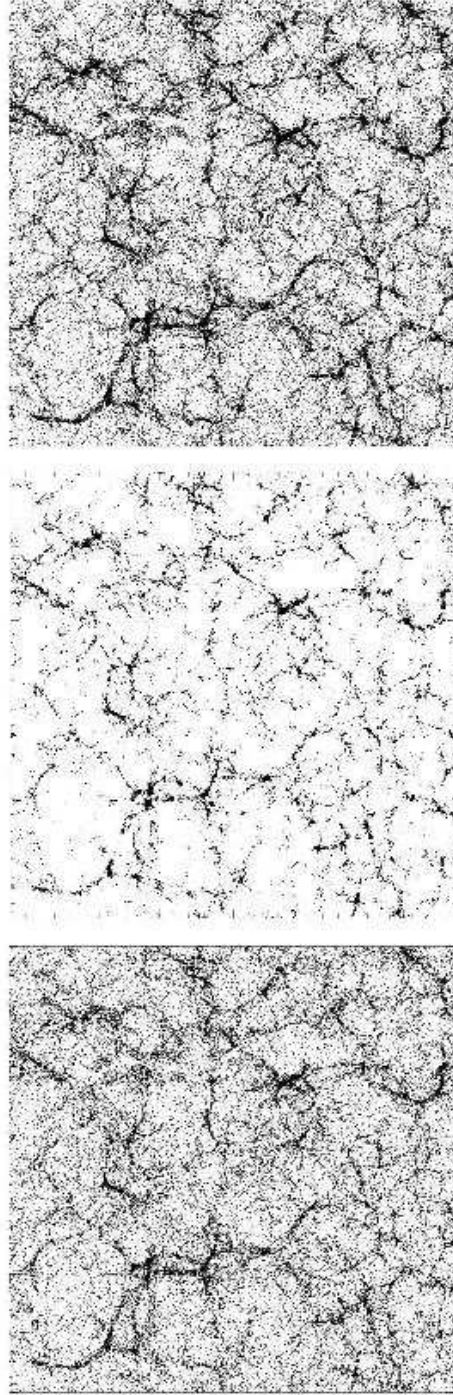
$$\rho(\mathbf{r}_g) = \frac{8M_p}{\pi R_{\text{sph}}^3(\mathbf{r}_g)} \sum_{i=1}^{N_{\text{sph}}} \zeta \left[ \frac{r_i}{R_{\text{sph}}(\mathbf{r}_g)} \right], \quad (1)$$

<sup>2</sup> downloaded from <http://www.qhull.org/>

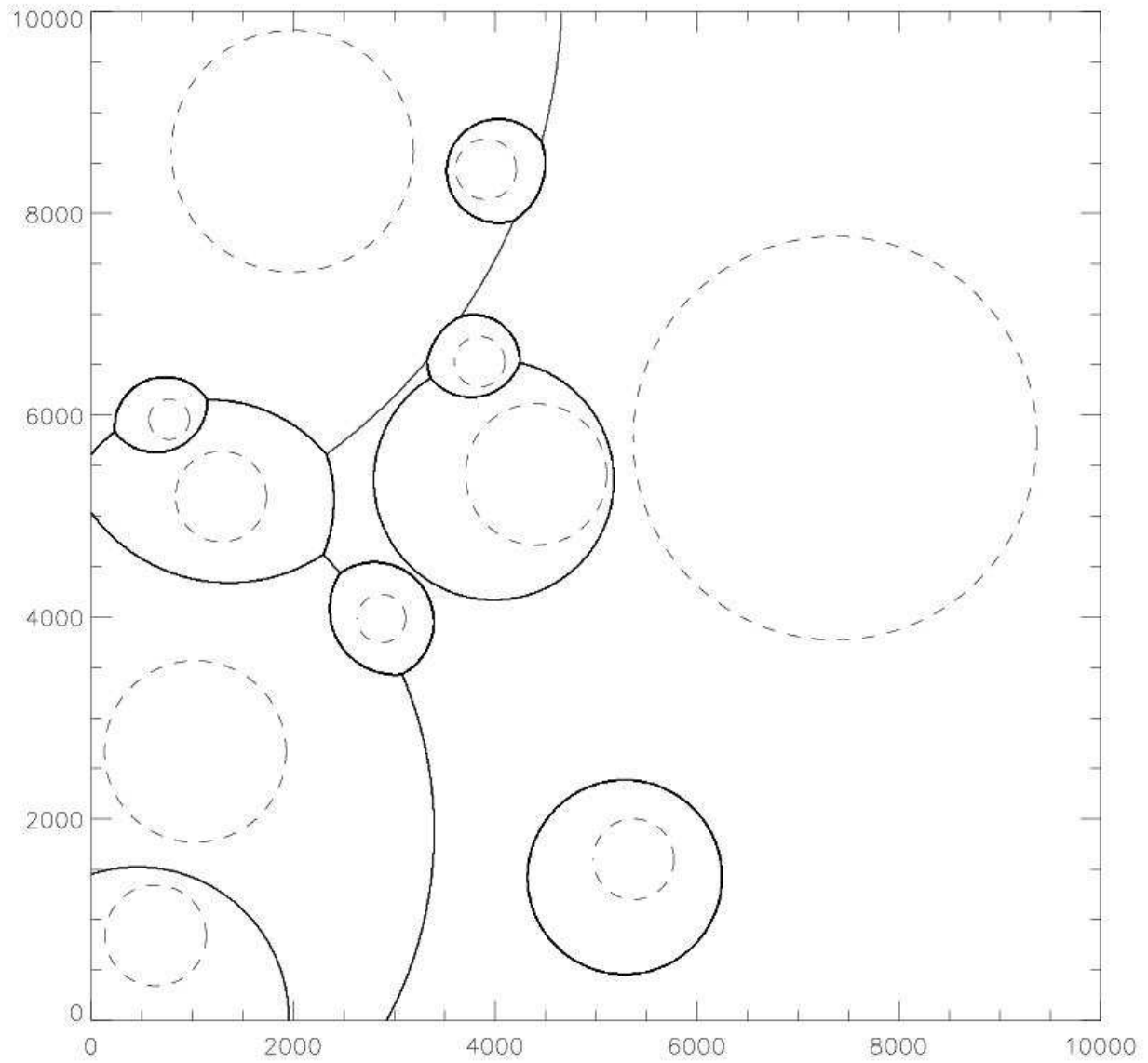
where  $R_{\text{sph}}(\mathbf{r}_g)$  is half the distance from  $\mathbf{r}_g$  to the farthest neighbor of the sub grid among the  $N_{\text{sph}}$  particles, and  $r_i$  is the distance of the  $i$ th particle to the sub grid site. Finally we average over the densities of all the  $7^3$  sub-grids to obtain the density of the corresponding ‘base-grid’.



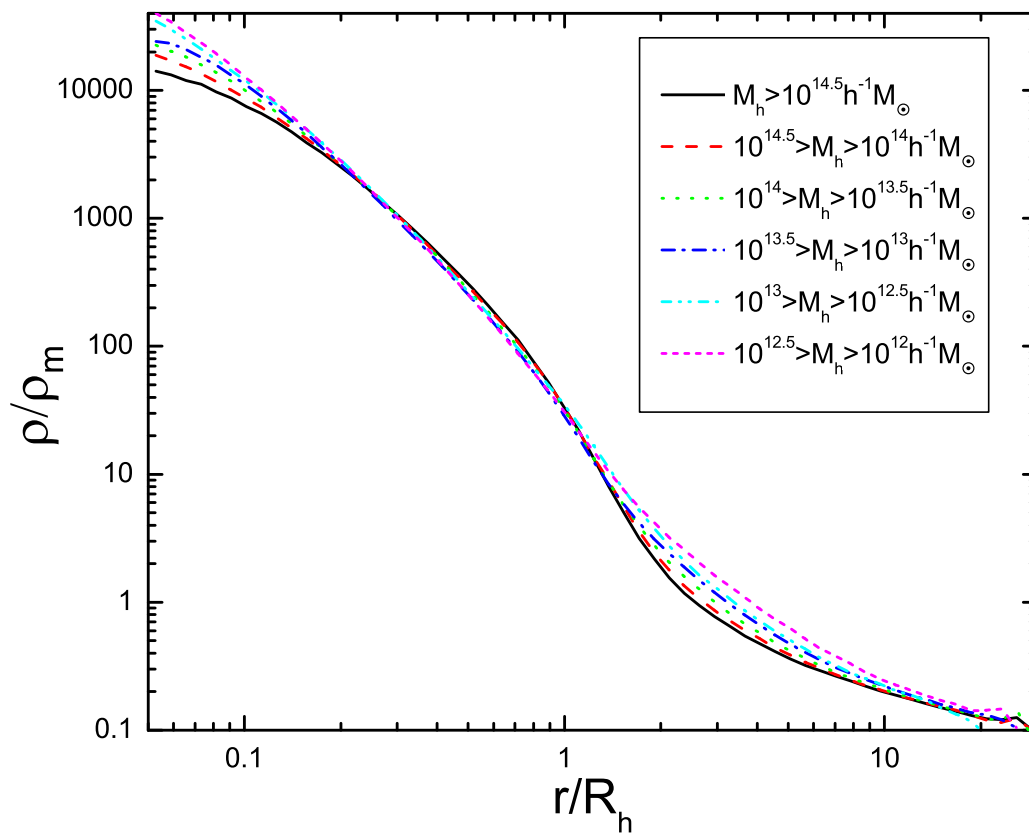
**Figure 1.** The fraction of cosmic mass contained in haloes with mass above  $M_h$  as a function of  $M_h$ .



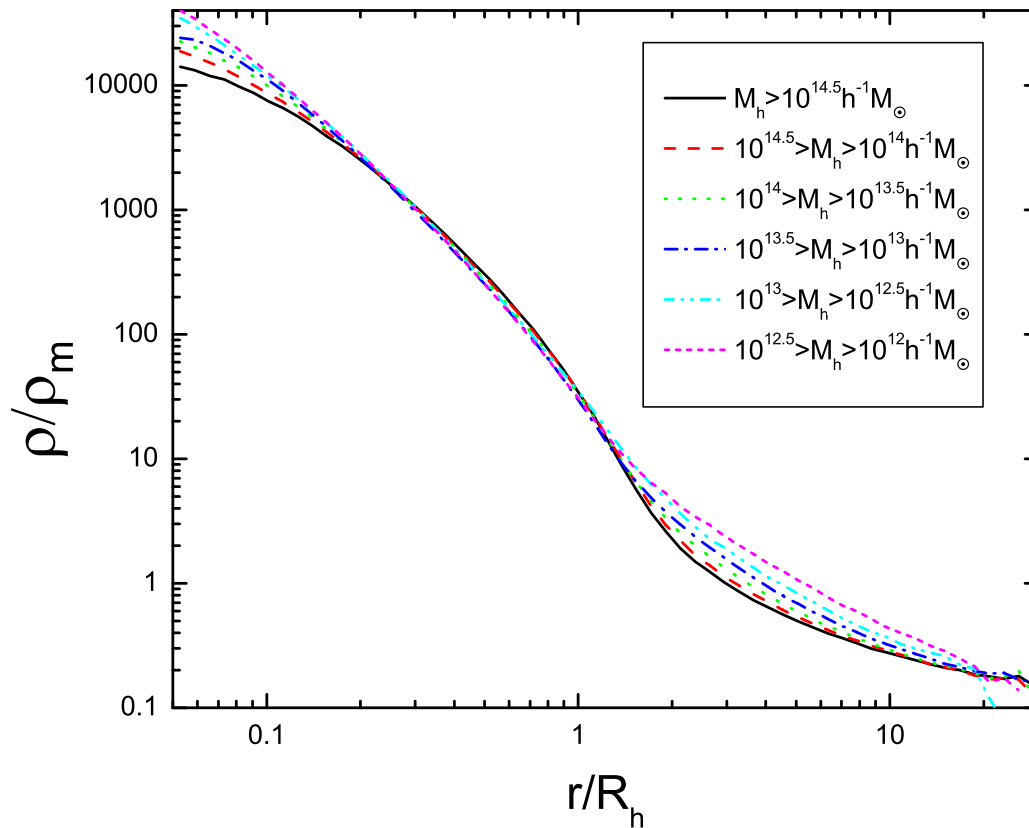
**Figure 2.** The distribution of all mass (upper panel), the mass in the halo population (middle panel) and the mass not in the halo population (lower panel) in a simulation slice of  $300 \times 300 \times 10 (h^{-1}\text{Mpc})^3$ . The haloes, shown here, have masses larger than  $10^{12} h^{-1} M_{\odot}$ .



**Figure 3.** The domain of randomly distributed haloes. The dashed lines represent the haloes, scaled by the virial radius of each halo. The solid lines are the boundaries of the domains (see text for details).

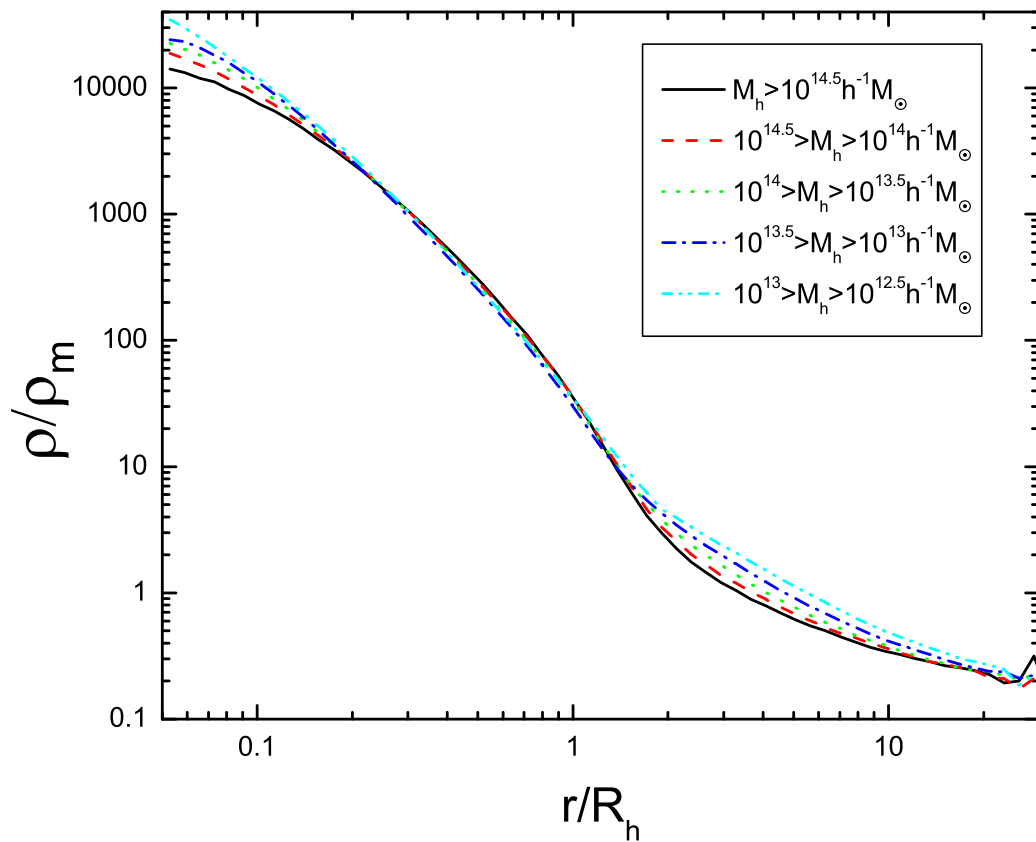


**Figure 4.** The density profiles of mass in and around the haloes in various mass bins. Here the mass threshold for the halo population is  $M_{\text{th}} = 1.68 \times 10^{11} h^{-1} M_{\odot}$ . The radius  $r$  is scaled by halo virial radius  $R_h$ , and the density is scaled with  $\rho_m$ , the mean density of the universe.

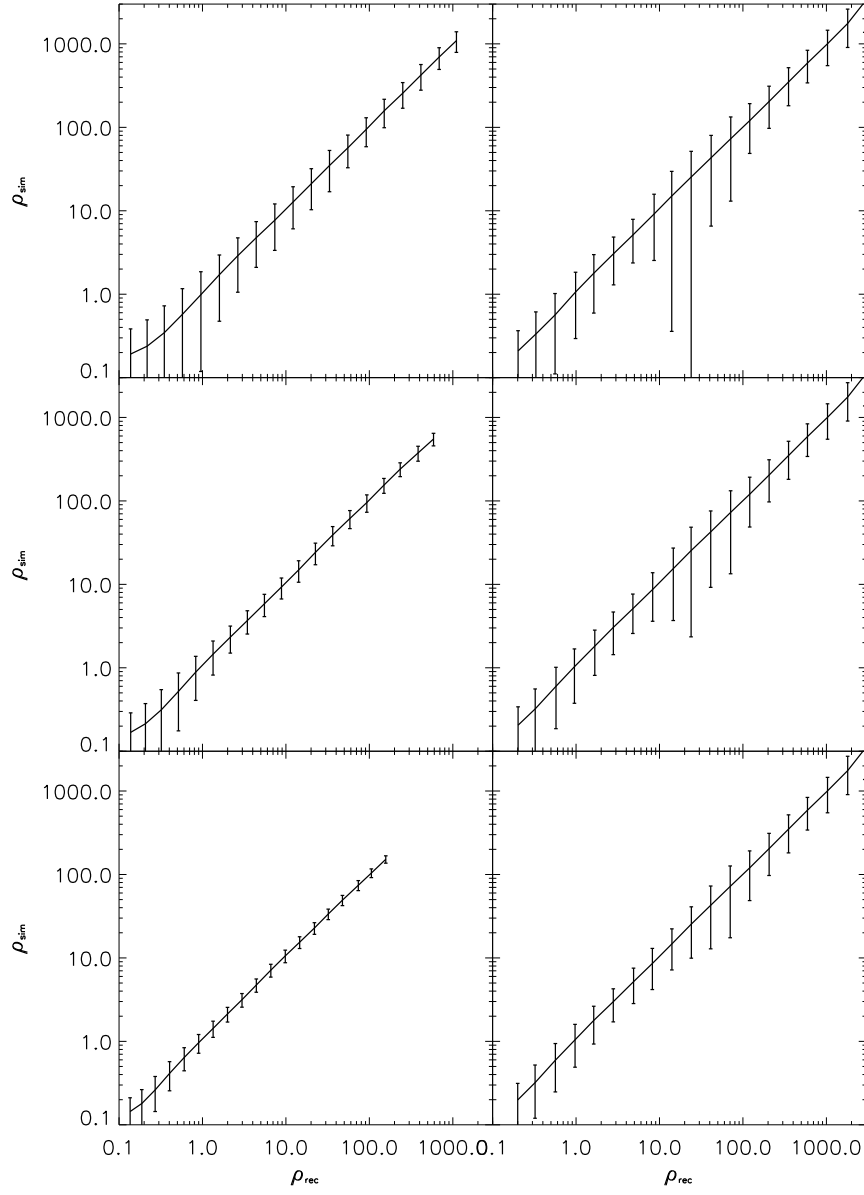


**Figure 5.** The density profiles of mass in and around the haloes in various mass bins. Here the mass threshold for the halo population is  $M_{\text{th}} = 1.0 \times 10^{12} h^{-1} M_\odot$ . The radius  $r$  is scaled by halo virial radius  $R_h$ , and the density is scaled with  $\rho_m$ , the mean density of the universe.

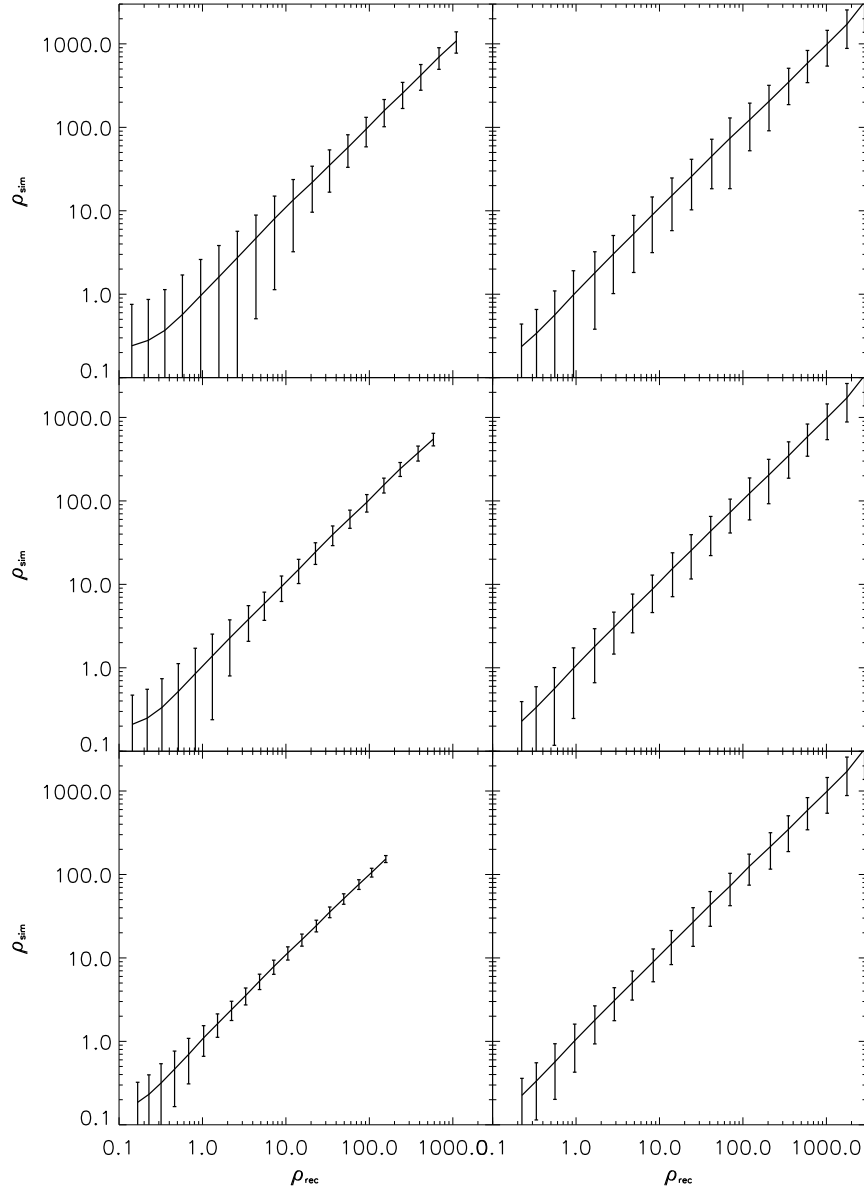




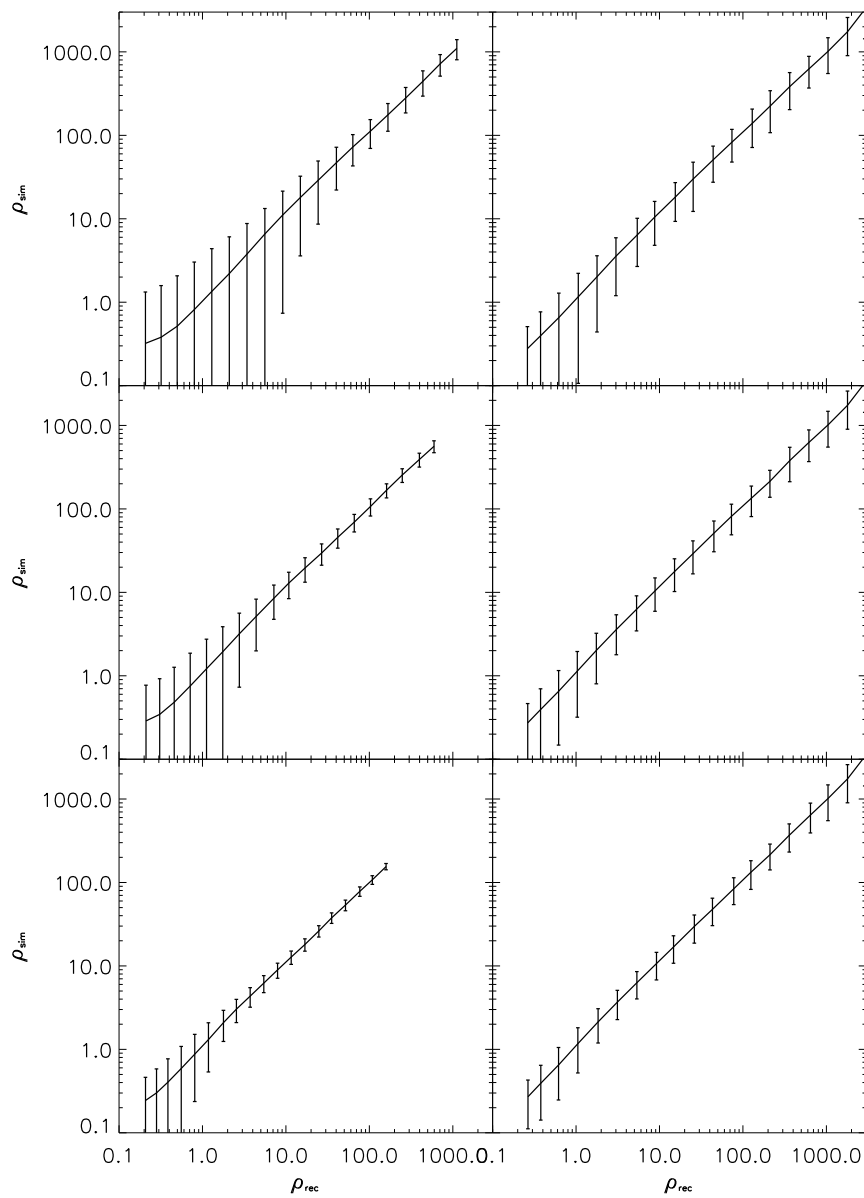
**Figure 6.** The density profiles of mass in and around the haloes in various mass bins. Here the mass threshold for the halo population is  $M_{\text{th}} = 1.0 \times 10^{12.5} h^{-1} M_{\odot}$ . The radius  $r$  is scaled by halo virial radius  $R_h$ , and the density is scaled with  $\rho_m$ , the mean density of the universe.



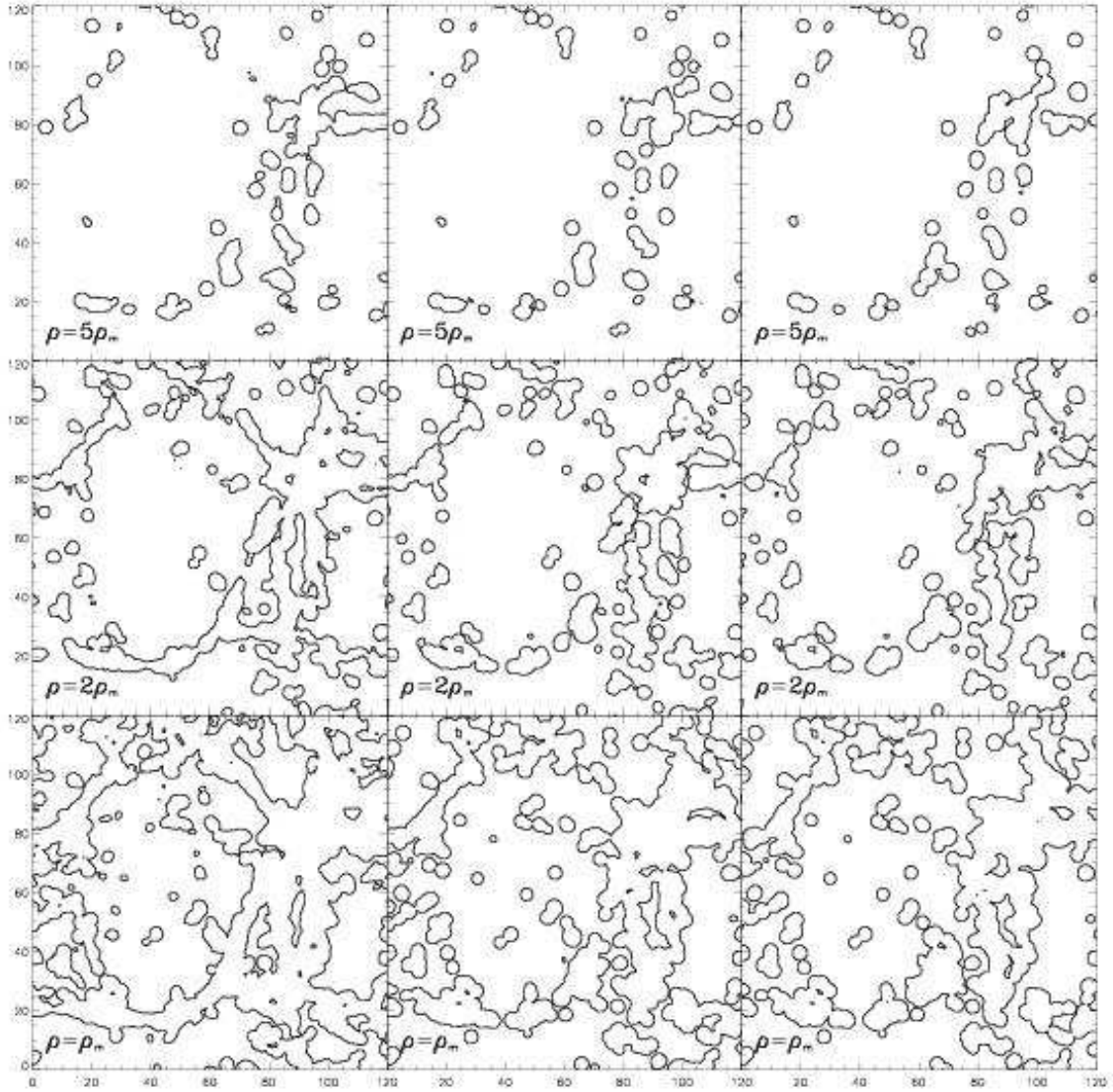
**Figure 7.** The comparison of density between the simulation and the reconstruction. The reconstruction here is obtained by using halo population with  $M_{\text{th}} = 1.68 \times 10^{11} h^{-1} M_{\odot}$  and density profiles shown in Fig. 4. In the three left panels, the density field is smoothed on a fixed length  $1 h^{-1} \text{Mpc}$ ,  $2 h^{-1} \text{Mpc}$  and  $4 h^{-1} \text{Mpc}$ . In the three right panels, the density field is smoothed with an adaptive length  $l_{\text{ad}}(M_{\text{th}}/2)$ ,  $l_{\text{ad}}(M_{\text{th}})$  and  $l_{\text{ad}}(2M_{\text{th}})$  (see text for the definitions of the smoothing length).



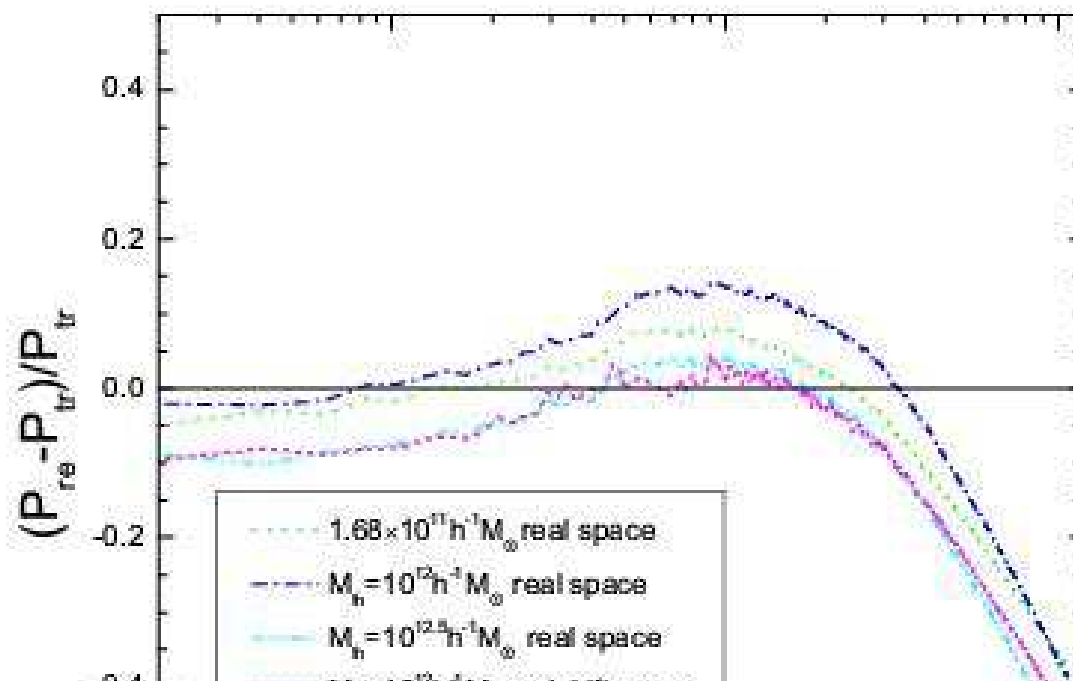
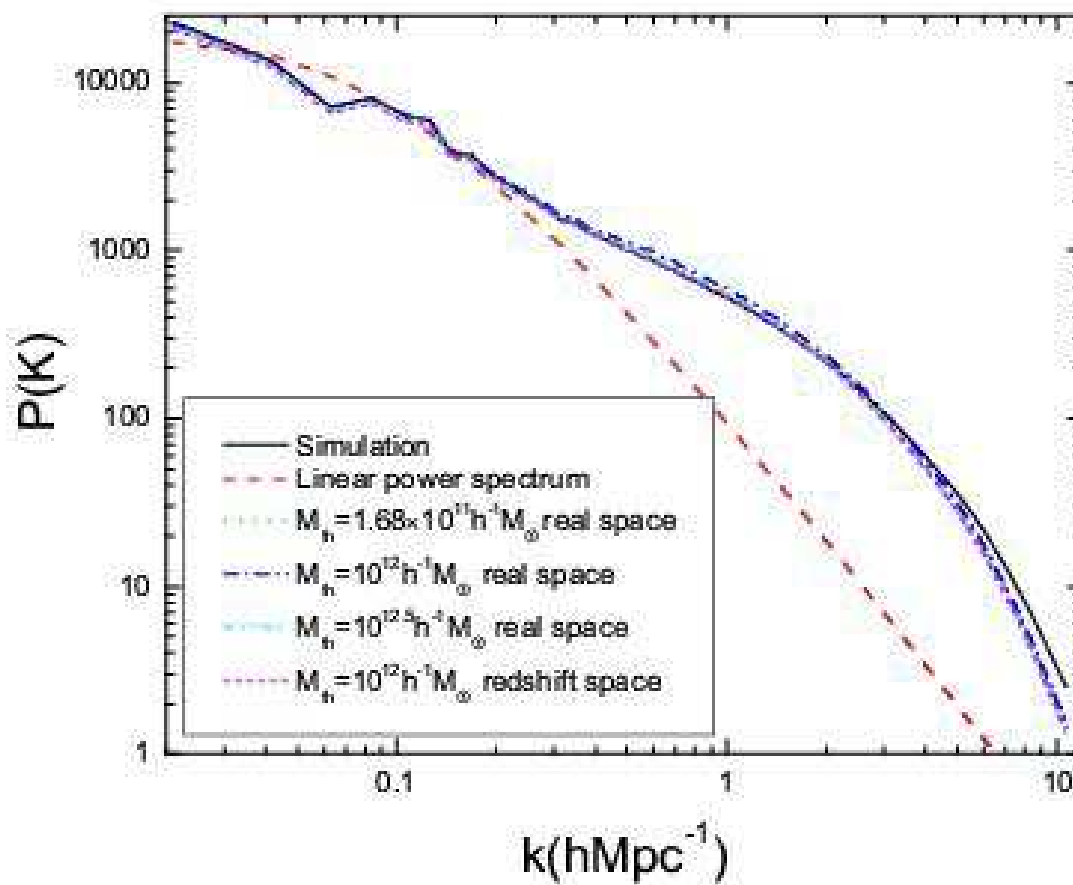
**Figure 8.** The same as Fig. 7 except  $M_{\text{th}} = 10^{12} h^{-1} M_{\odot}$ .



**Figure 9.** The same as Fig. 7 except  $M_{\text{th}} = 10^{12.5} h^{-1} M_{\odot}$ .



**Figure 10.** The contours at three density levels (as indicated in the panels) of the dark matter distribution in a slice of  $120 \times 120 \times 10 (h^{-1} \text{Mpc})$ . The left panels show the result for simulation, the middle and right panels are for the reconstructions based on haloes in real space and in redshift space, respectively. The two reconstructions are made using halo population with  $M_{\text{th}} = 10^{12} h^{-1} M_{\odot}$ . The contours are based on the projections of cubes of  $4 h^{-1} \text{Mpc}$  on a side, in which the density is above the density threshold.



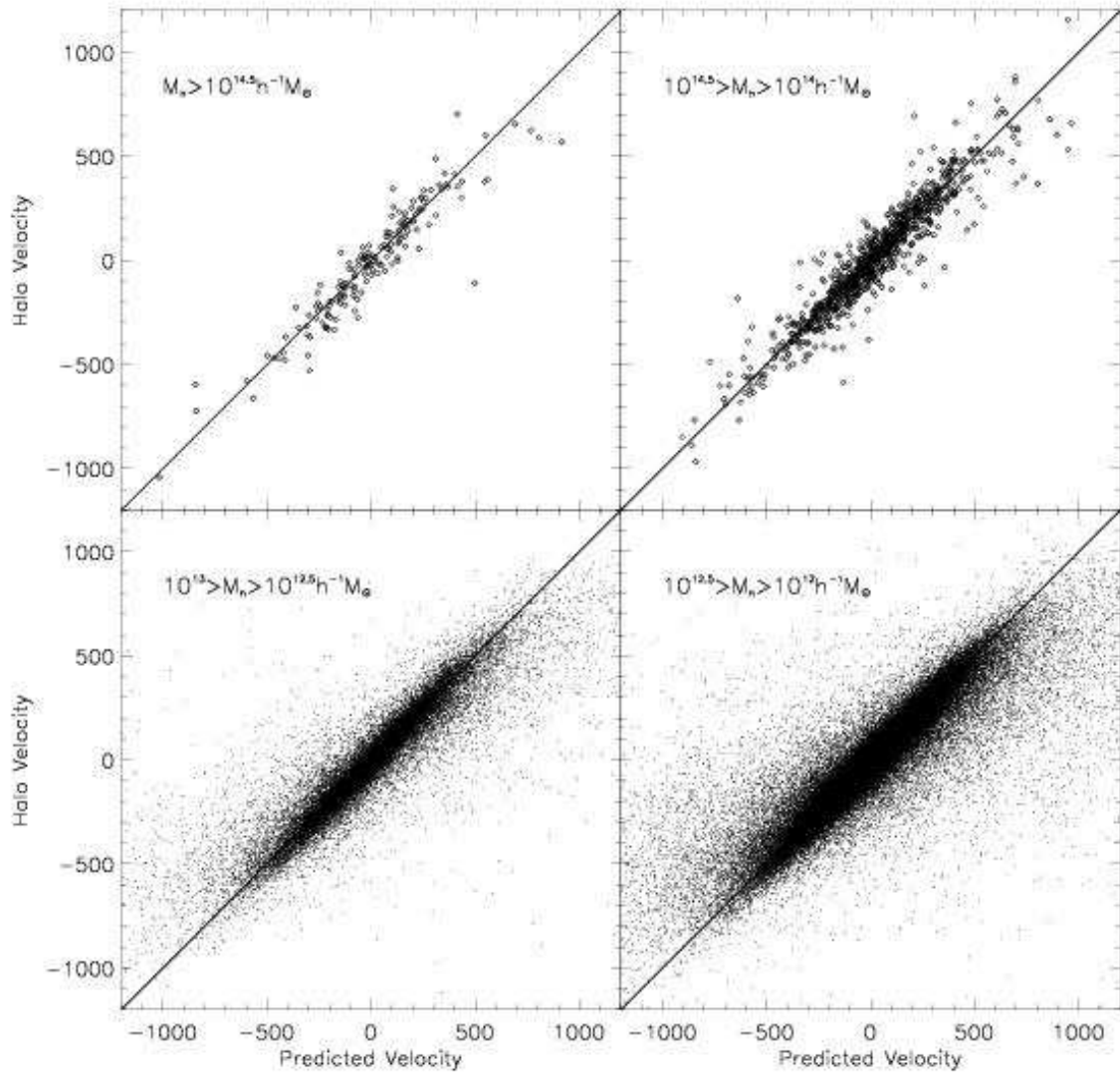


**Figure 12.** The  $x$ -component of the halo velocity obtained from the simulation against the corresponding predicted velocity by applying linear theory on the reconstructed density field from haloes with masses above  $M_{\text{th}} = 1.0 \times 10^{12} h^{-1} M_\odot$  distributed in the real space.

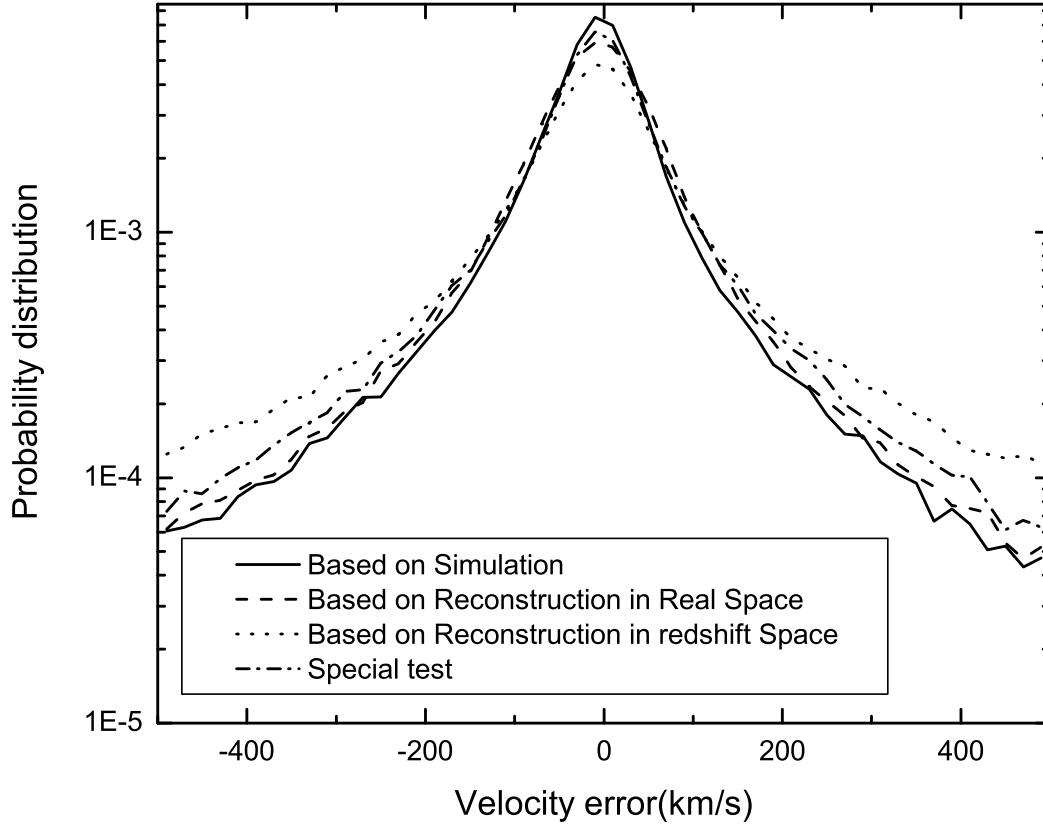


**Figure 13.** The probability distribution of the difference between the predicted velocity and the real velocity. The solid line represents the predicted velocity based on the mass distribution in the original simulation(L300). The dash and dot lines represent the predicted velocity based on reconstructions in real space and redshift space, respectively. Both reconstructions are made with haloes with masses above  $10^{12} h^{-1} M_{\odot}$ . For comparison, we also show the distribution of the velocities calculated at the real positions of halos but using the reconstructed density field from redshift-space data (dash-dot line; see the text for details).



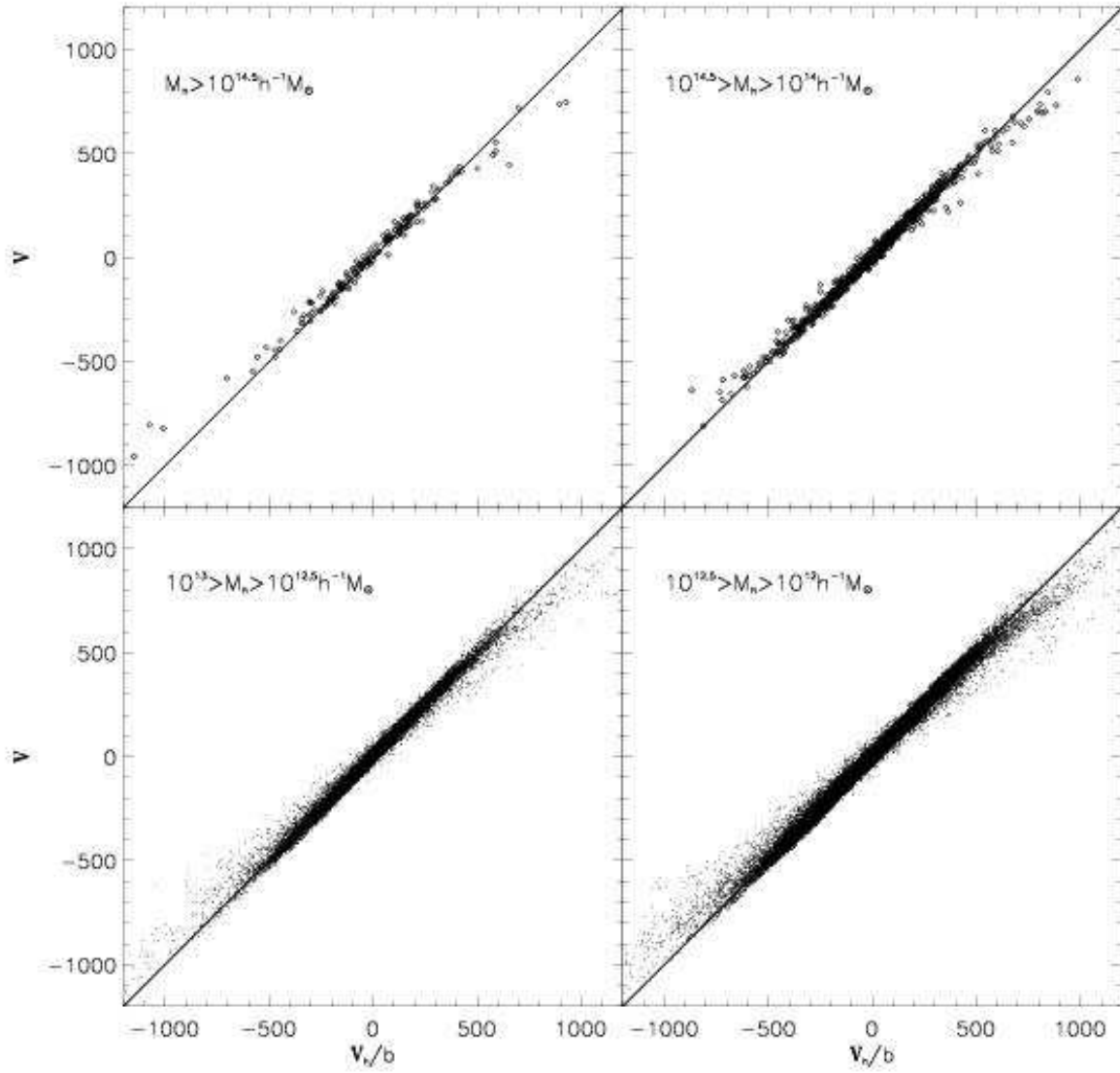


**Figure 14.** The predicted velocity,  $\mathbf{v}_h$ , based on halo population with masses above  $10^{12} h^{-1} M_\odot$  in real space versus  $\mathbf{v}$ , the predicted velocity based on the original simulated mass distribution. Here a bias factor  $b = 1.56$  is used to scale  $\mathbf{v}_h$ , and a smoothing mass scale (SMS) of  $10^{14.75} h^{-1} M_\odot$  is used.

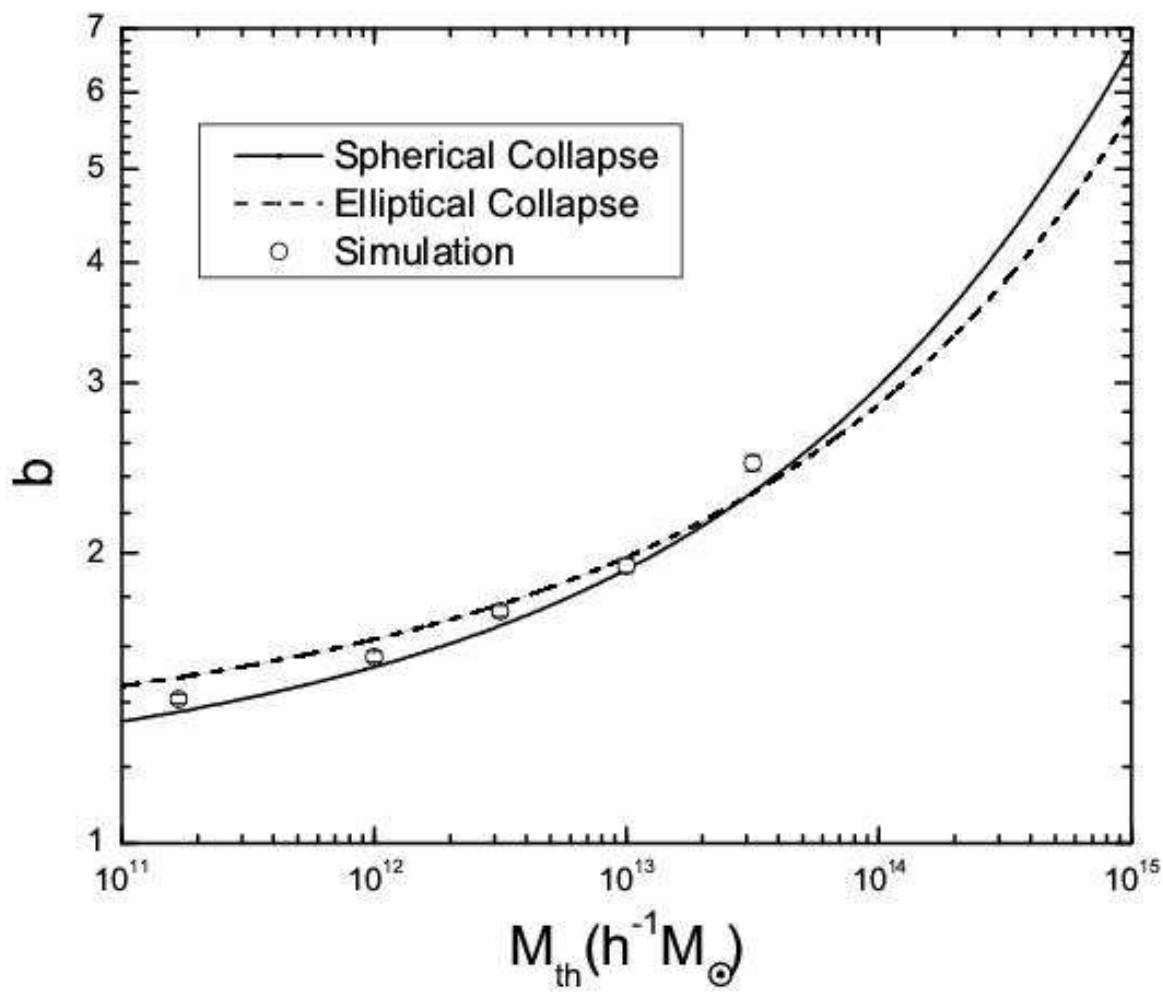


**Figure 15.** The bias parameter  $b$  (defined in the text) as a function of the mass threshold  $M_{\text{th}}$  for spherical collapse and elliptical collapse models indicated in the panel. For comparison we also show the results obtained directly from the simulation.

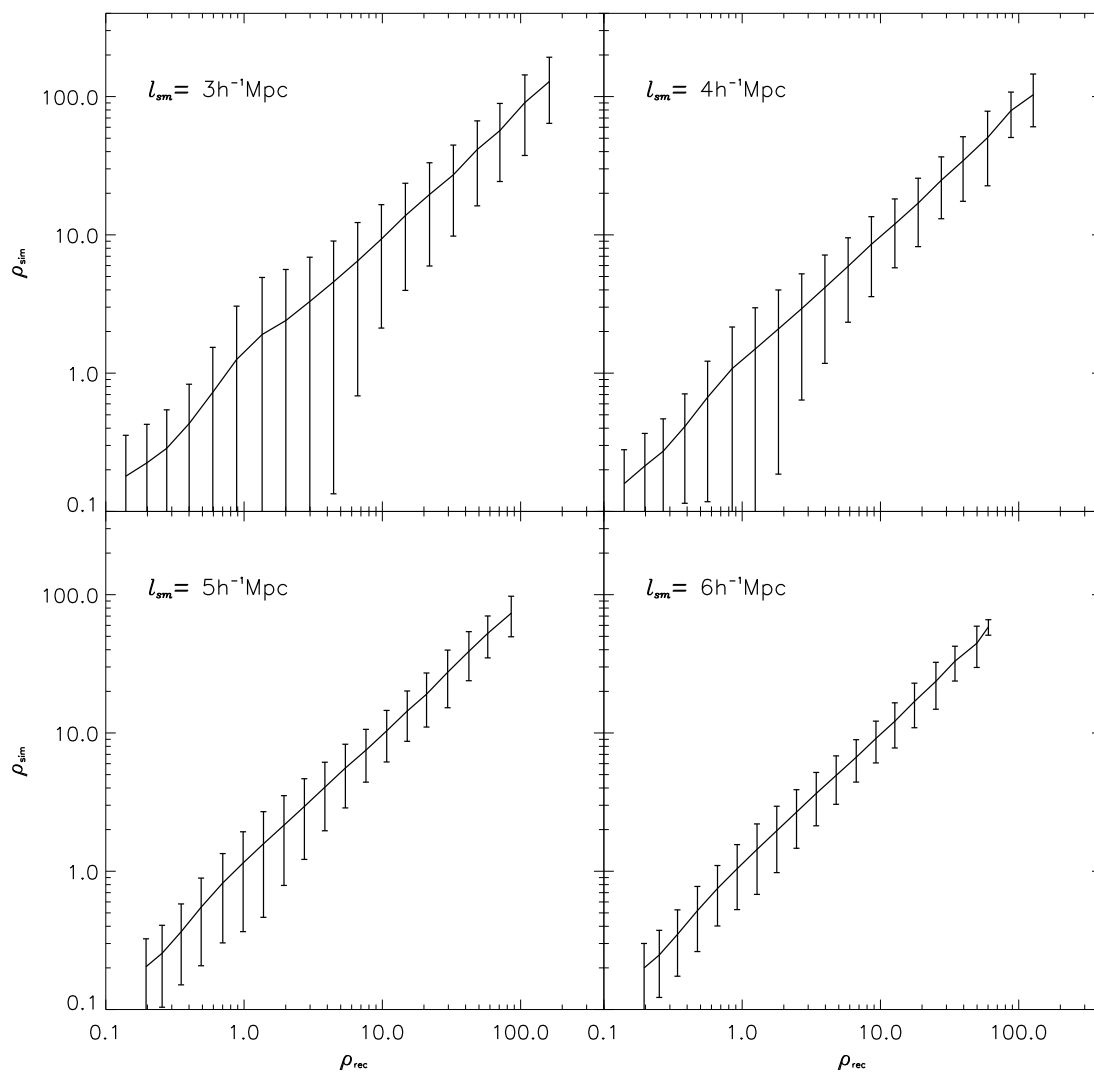


**Figure 16.** The reconstructed density based on the halo population with  $M_{\text{th}} = 10^{12} h^{-1} M_{\odot}$  in the redshift space versus the original density in the simulation. A fixed smoothing length is used in each panel as indicated.

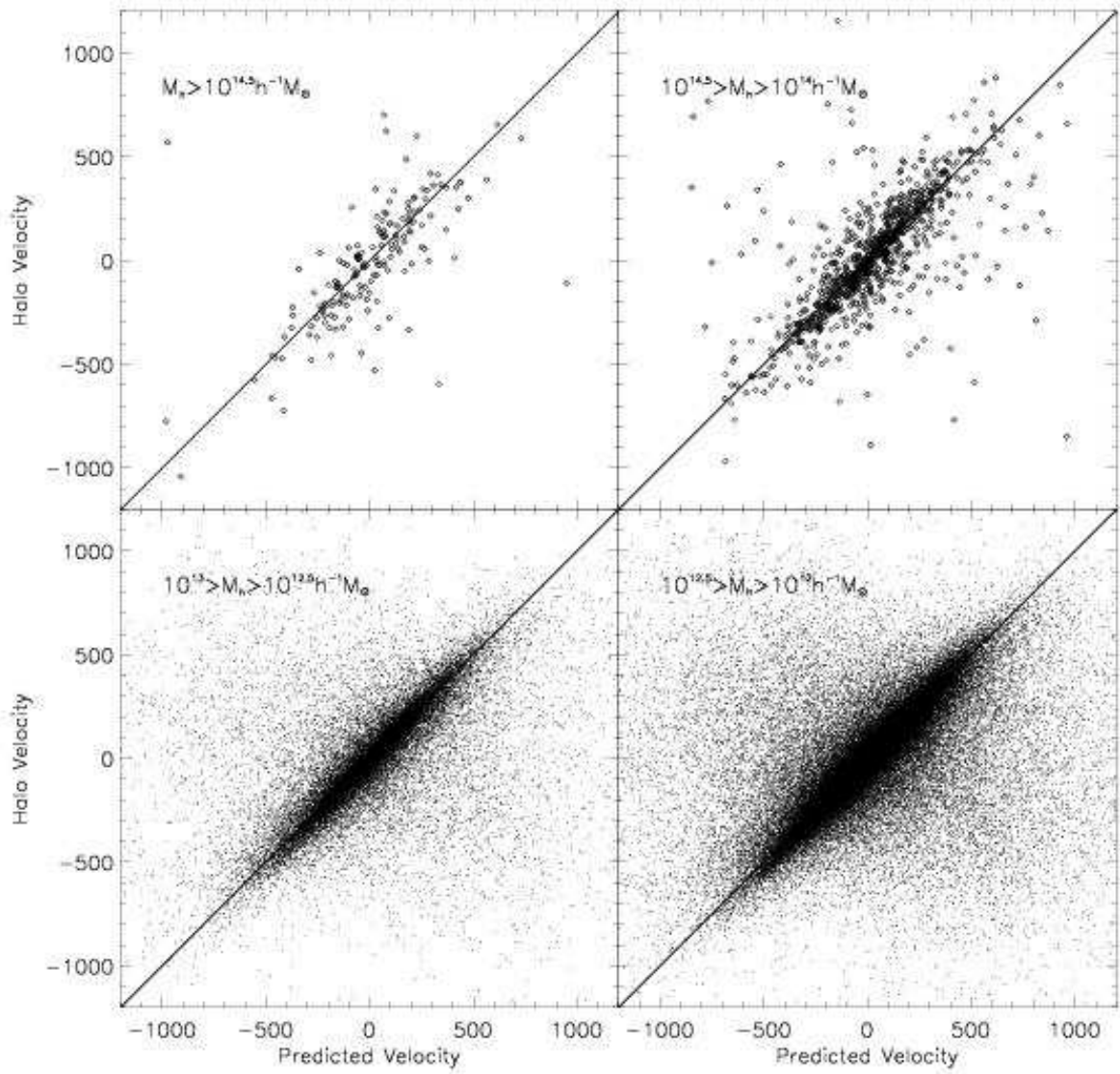


**Figure 17.** The same as Fig. 12 but the reconstruction is based on haloes distributed in redshift space.

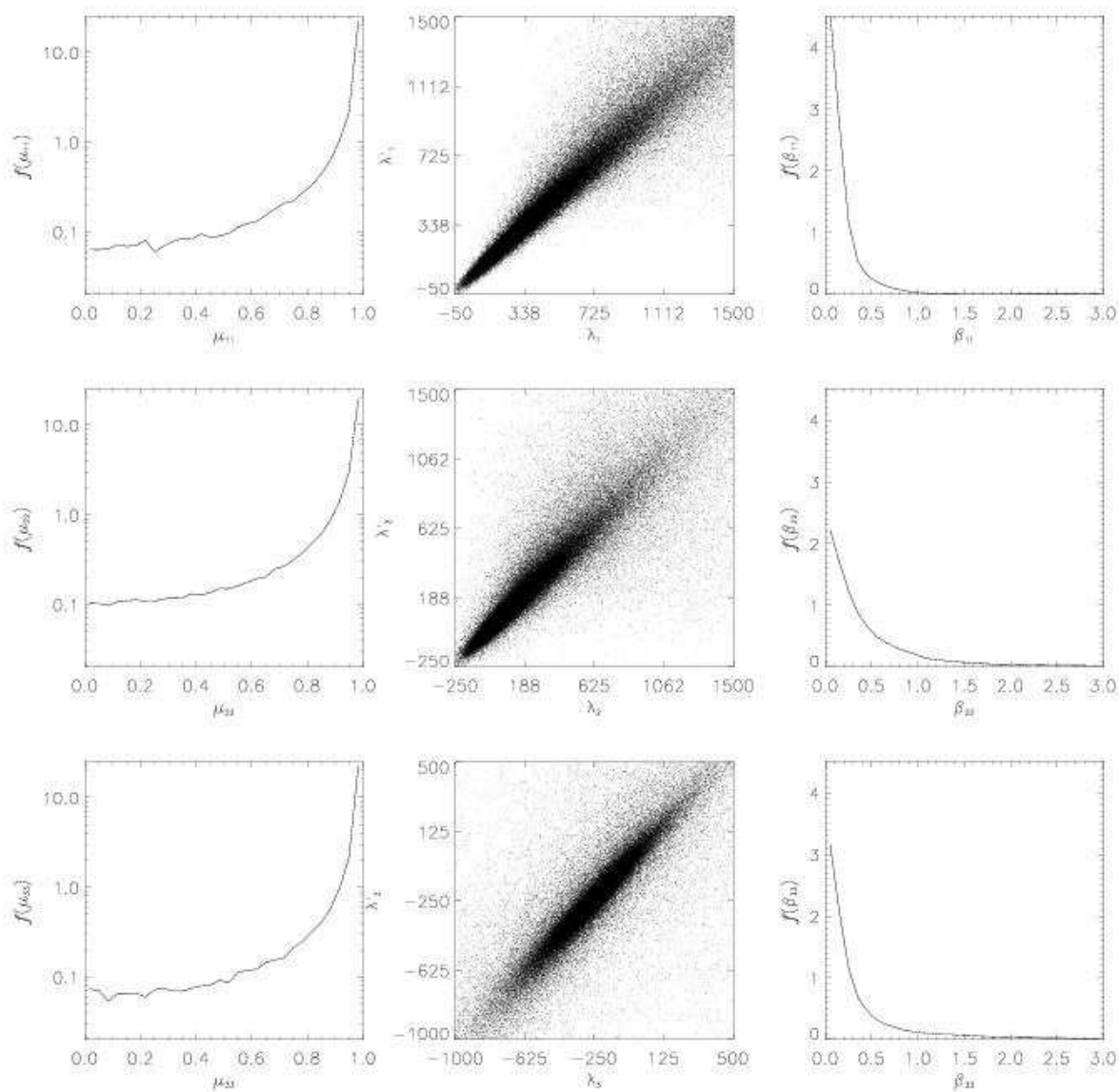


**Figure 18.** The comparison between the tidal field obtained from the reconstructed density field (based on haloes above  $10^{12} h^{-1} M_{\odot}$  in redshift space) and that from the original simulation. The three left panels show the distribution of the dot product  $\mu_i$  between  $\mathbf{d}'_i$  and  $\mathbf{d}_i$ . The three middle panels show  $\lambda'_i$  vs  $\lambda_i$ . And the three right panels are the distribution of  $\beta_i$  (see the text for the definition).